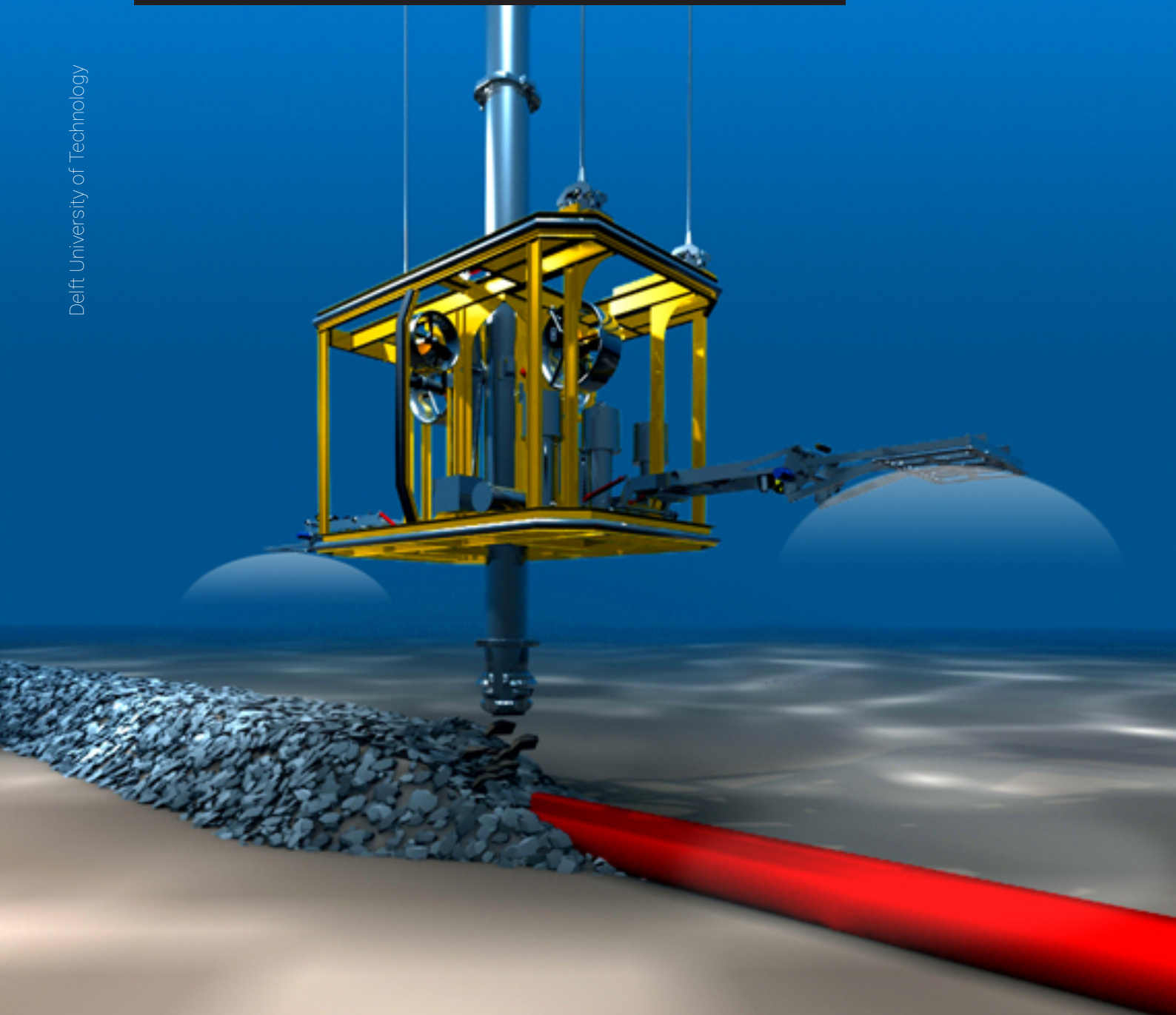


Reduction of the outflow velocity of a closed fallpipe system

The concept selection and analysis of an outflow velocity reduction mechanism

J. Reinders

Delft University of Technology



Reduction of the outflow velocity of a closed fallpipe system

The concept selection and analysis of an outflow velocity reduction mechanism

by

J. Reinders

to obtain the degree of Master of Science
at the Delft University of Technology,
to be defended publicly on Tuesday March 27, 2018 at 01:00 PM.

Student number:	4140087	
Project duration:	May 1, 2017 – March 27, 2018	
Thesis committee:	Prof. dr. ir. C. van Rhee,	Chairman, TU Delft
	Dr. ir. G. H. Keetels,	Daily Supervisor, TU Delft
	Dr. ir. H. J. de Koning Gans,	TU Delft
	Ir. C. Visser,	Supervisor, Tideway Offshore Solutions
	Ir. J. Willems,	Daily Supervisor, Tideway Offshore Solutions

This thesis is confidential and cannot be made public until March 27, 2023.

An electronic version of this thesis is available at <http://repository.tudelft.nl/>.

Abstract

DELFT UNIVERSITY OF TECHNOLOGY
TIDEWAY OFFSHORE SOLUTIONS

Master of Science Offshore and Dredging Engineering
Reduction of the outflow velocity of a closed fallpipe system
by J. Reinders

Subsea rock installation is widely applied in the offshore industry and utilized for a wide range of purposes including but not limited to: pipeline protection, scour protection, insulation of pipelines, upheaval buckling prevention and seabed preparation. Tideway Offshore Solutions is specialized in subsea rock installation and currently operates three state-of-the-art fallpipe vessels. Their vessel 'Flintstone' makes use of an innovative closed fallpipe system to provide high accuracy subsea rock installation.

The presence of rocks in the water column of the fallpipe increase the density of the mixture in the fallpipe. The density difference between the mixture in the fallpipe and the density of the surrounding sea-water results in a water level drop in the fallpipe. To keep this water level drop within acceptable limits extra water is added to the fallpipe system which accelerates the fallpipe flow. The accelerated fallpipe flow can result in high outflow velocities of the rock mixture at the fallpipe exit. High outflow velocities of the rock mixture can eventually result in increased impact velocities of the rock particles on the seabed. Increased impact velocities of the rock particles on the seabed can lead to unsatisfactory rock berm shapes resulting in the need for remedials. To have their fallpipe system perform as efficient as possible Tideway Offshore Solutions was interested in possible measures to reduce the outflow velocity of the fallpipe which resulted in this thesis.

In the first part of this thesis different concepts, that could potentially reduce the outflow velocity of the fallpipe, are generated and conceptually analyzed. The information acquired from this analysis is used as input for a multi criteria analysis that resulted in the selection of the most promising concept, the use of a deflector. The deflector will act as a flow deflector at the fallpipe exit thereby decreasing the impact velocity of rock particles on the seabed. In the second part of this thesis a complete three-dimensional computational fluid dynamics (CFD) analysis is performed on the fallpipe outflow with and without deflector. The CFD program used to simulate these situations is ANSYS Fluent. The simulations for both cases are performed for two different turbulence models, the $k - \epsilon$ and $k - \omega SST$ turbulence models, the distance from the fallpipe exit to the seabed is varied as well and a range of deflector angles and dimensions are simulated.

The fluid flow velocities obtained from the CFD analysis are used as input in a MATLAB model to compute the rock particle trajectories in a two-dimensional plane. Combining the rock particle trajectories and their velocity components it is possible to compute the impact velocities of the rock particles on the seabed. The results of the trajectory model set up in MATLAB showed that a substantial decrease in impact velocity of the rock particles on the seabed can be achieved by using a deflector at the fallpipe exit.

Preface

The report you have in front of you at the moment is the master thesis that I wrote to fulfill all the requirements to finalize my Master in Science in Offshore & Dredging Engineering at Delft University of Technology. The desire of Tideway Offshore Solutions to find a way to reduce the outflow velocity of their closed fallpipe system is what initiated this study. During the last eleven months the quest for finding and analyzing a solution to reduce the outflow velocity of the closed fallpipe system has kept me busy and challenged me in many ways. I am extremely thankful for the chance Tideway Offshore Solutions gave me to conduct my thesis research within their company.

Within Tideway Offshore Solutions I would like to express my gratitude towards: Joost Willems my daily supervisor, Connie Visser, Sanne Crum who stepped in as daily supervisor in the early phase of my thesis when Joost was still working abroad and of course all the other colleagues from the Engineering Department. Furthermore, I would like to thank professor Cees van Rhee and Geert Keetels from Delft University of Technology for their valuable input during the meetings.

Finally, I want to use this possibility to thank my family and friends for their support during the entire duration of my studies in Delft. Your support has been extremely valuable and helped me to get to where I am now.

*J. Reinders
Breda, March 2018*

Contents

Abstract	iii
Preface	v
Contents	viii
List of Figures	ix
List of Tables	xi
Nomenclature	xiii
1 Introduction	1
1.1 General Introduction	1
1.2 Problem Definition	1
1.3 Objective	3
1.4 Approach	3
2 Subsea Rock Installation	5
2.1 Areas of Application.	5
2.2 Tideway's 'Flintstone' Rock Placement Vessel	6
3 Rock Properties	7
3.1 Rock Types	7
3.2 Rock Mass and Size	7
3.3 Rock Shape	8
3.4 Rock Grading	9
4 Rock Installation	11
4.1 Single Rock Installation	11
4.2 Multiple Rock Installation.	12
4.3 Fallpipe Rock Installation	13
4.3.1 Flexible Fallpipe System	13
4.3.2 Closed Fallpipe System.	14
4.3.3 Impact Assessment	14
5 Fallpipe Outflow	17
5.1 Circular Turbulent Jet	17
5.2 Free Jet Region	18
5.3 Impinging Jet Region	19
5.4 Wall Jet Region	21
6 Conceptual Measures to Reduce Fallpipe Outflow Velocities	25
6.1 Concept Generation	25
6.2 Concept Selection.	25
6.2.1 Concept Screening.	25
6.2.2 Multi Criteria Analysis	25
6.2.3 Result	25
7 Computational Fluid Dynamics Analysis	27
7.1 Simulation Plan	27
7.2 Mesh Independency Study	28
7.3 Set-up.	28
7.4 Impinging Jet	31
7.4.1 Impinging Jet - Validation	35

7.5	Deflector	38
7.6	Conclusion & Results	38
8	Rock Trajectory Model	39
8.1	Input & Model Structure	39
8.2	Output	42
8.3	Velocity Magnitude Tracking	42
8.4	Conclusion & Results	42
9	Conclusion & Recommendations	43
	Bibliography	45
A	Appendix A: Airlift	49
B	Appendix B: Multi Criteria Analysis	51
B.1	Criteria & Grading System.	51
B.2	Weighting of the Criteria	51
B.3	Normalization of the Weighing Factors	51
B.4	Score Sheet MCA	51
C	Appendix C: Python-program structure	53
D	Appendix D: Mesh Independency Study	55
D.1	Mesh Generation	55
D.2	Near-Wall Treatment	57
D.3	Problems	59
E	Appendix E: Serial Numbers	63
F	Appendix F: Results CFD Simulations	65

List of Figures

1.1	Area of interest	3
2.1	Area's of application [Tideway Internal Images]	5
2.2	A) Side-stone dumping vessel, B) Split hopper barge, C) Fallpipe vessel, D) Dragline [Kevelam]	6
3.1	LT ratio measurement [CIRIA; CUR; CETMEF, 2007]	8
5.1	Definitions of jet regions	18
5.2	Normalized centerline velocity for the free jet region	19
5.3	Normalized centerline velocity impinging jet region (large SOD)	20
5.4	Normalized centerline velocity impinging jet region (small SOD)	21
5.5	Normalized maximum horizontal velocity wall jet region (large SOD)	22
5.6	Normalized maximum horizontal velocity profile wall jet region (large SOD)	22
5.7	Normalized maximum horizontal velocity wall jet region (small SOD)	23
7.1	Velocity profile development fallpipe length section of $4 \cdot D$	27
7.2	Normalized centerline velocities for different input velocities and SOD	32
7.3	Normalized radial velocities for different input velocities and radial location	32
7.4	Normalized radial velocities for different k_s values and radial location	33
7.5	Normalized centerline velocities for different turbulence models and SOD	33
7.6	Normalized radial velocities for different turbulence models and radial location	34
7.7	Contour plots TKE for different turbulence models with SOD = 10 D	34
7.8	Contour plots TKE for different turbulence models with SOD = 17.5	35
7.9	Turbulent kinetic energy for different turbulence models and location in the flow field	35
7.10	Normalized centerline velocity comparison for the free jet region	36
7.11	Normalized centerline velocity comparison for the impinging jet	36
7.12	Normalized horizontal velocity comparison for the wall jet region, SOD = 10, $k - \epsilon$ model	37
7.13	Normalized horizontal velocity comparison for the wall jet region, SOD = 10, $k - \omega SST$ model	38
D.1	Centerline Velocity - Mesh Independency Study	56
D.2	Monitor Points - Mesh Independency Study	57
D.3	Subdivisions of the near-wall regions [ANSYS, 2018a]	58
D.4	Returning oscillating residuals for mesh refinement	59
D.5	Locations of the Monitor Points in the Simulation Domain	59
D.6	Illustration of the local mesh refinement	60
D.7	Influence of local refinement on residuals	61
D.8	Influence of local refinement on flow development	61
D.9	Extended flow domain of oscillatory mesh (SOD = 15)	62
E.1	The different configurations of the CFD simulations with their respective serial numbers	63

List of Tables

3.1	The three main grading widths [CIRIA; CUR; CETMEF, 2007]	9
3.2	Grading classes used by Tideway [Internal Information Tideway]	9
4.1	Impact velocity and energy according to “Method I”	15
7.1	Result Mesh Independency Study	28
7.2	Model constants for the $k - \varepsilon$ turbulence model	30
7.3	Model constants for the $k - \omega SST$ turbulence model	31

Nomenclature

Abbreviations

CFD	Computational Fluid Dynamics
DP	Dynamic Positioning
kts	nautical miles per hour
LTP	Lower Telescopic Pipe
MCA	Multi Criteria Analysis
MPV	Multi Purpose Vessel
ROV	Remotely Operated (underwater) Vehicle
SOD	Stand-Off Distance
t	metric ton
WIP	Water Inlet Pipes

Greek Symbols

Δ	specific density	[-]
μ_t	eddy viscosity	$[m^2/s]$
ν	kinematic viscosity	$[m^2/s]$
ω	specific turbulence dissipation rate	$[1/s]$
ρ	density	$[kg/m^3]$
τ_e, τ	characteristic eddy lifetime	[-]
ε	turbulence dissipation rate	$[m^2/s^3]$
ζ	normally distributed random number	[-]
ζ_{carnot}	carnot loss coefficient	[-]
ζ_{wall}	wall loss coefficient	[-]

Roman Symbols

A	area	$[m^2]$
A_{fp}	fallpipe exit cross-sectional area	$[m^2]$
A_p	area of particle subjected to flow resistance	$[m^2]$
C, C_v	volumetric concentration	[-]
c_{air}	concentration of air	[-]
C_D	drag coefficient	[-]
C_L	integral time scale constant	[-]

D, d	diameter	[m]
D_H	hydraulic diameter	[m]
E_{imp}	impact energy	[J]
F_b	buoyancy force	[N]
F_D	drag force	[N]
F_g	gravitational force	[N]
F_s	shape factor	[-]
g	gravitational acceleration	$[m/s^2]$
I	Impuls	[N s]
k	turbulence kinetic energy	$[m^2/s^2]$
k_s	roughness height	[m]
L	characteristic length	[m]
l	turbulence length scale	[m]
L_{eff}	effective fallpipe bucket length	[m]
L_p	Fallpipe length	[m]
M, m	mass	[kg]
M_a, m_a	added mass	[kg]
n	hindered settling factor	[-]
P	Production	[t/h]
$P_{c,iso}$	air compressor power	[kW]
$p_{driving}$	driving force in fallpipe	[Pa]
$p_{fric,total}$	frictional force in fallpipe	[Pa]
P_r	Production rate	[kg/s]
$Q_{G,atm}$	air compressor volumetric flow rate	$[m^3/s]$
r_1	distance to inner edge annular shear layer	[m]
Re	Reynolds number	[-]
T_L	integral time scale	[s]
t_p	particle relaxation time	[s]
U	characteristic velocity	[m/s]
u_0	uniform velocity at fallpipe exit	[m/s]
V	volume	$[m^3]$
$v_{equilibrium}$	terminal settling velocity of individual rock particle	[m/s]
v_{exit}	velocity of rock particles at fallpipe exit	[m/s]
v_e	particle velocity	[m/s]

v_{hs}	hindered settling velocity	[m/s]
v_{imp}	impact velocity	[m/s]
V_p	volume of the particle	[m^3]
v_{ts}	terminal settling velocity	[m/s]
v_{water}	water velocity at fallpipe exit	[m/s]
v_w	water velocity	[m/s]
W	weight	[kg]
x_{ch}	characteristic length for fully established flow	[m]

Subscripts

50	median
c	centerline
f	fluid
max,m	maximum
min	minimum
$n50$	median nominal
p	particle
s	solid
w	water



Introduction

1.1. General Introduction

Subsea rock installation is widely applied in the offshore industry. It is used for a wide range of purposes, examples are: pipeline protection, scour protection, insulation of pipelines, upheaval buckling prevention and seabed preparation. This technique is applicable to a range of water depths. The two main water depth ranges are: shallow subsea rock installation (up to 50 meters water depth) and subsea rock installation at greater water depths (50 to approximately 2000 meters).

In shallow water the primarily used technique for subsea rock installation is side-stone dumping. This is a simple method however its accuracy is limited and quickly deteriorates for increasing water depths. In greater water depths fallpipes are used to guide the rocks from the water surface to their designated position on the seabed. One can distinguish two different types of fallpipes: closed- and open fallpipe systems. This thesis will focus on the closed fallpipe system, since this system is in use at Tideway Offshore Solutions.

Tideway Offshore Solutions is based in Breda, the Netherlands and is part of the international DEME-Group. With its expertise the company serves the entire offshore energy market. Tideway is specialized in landfall construction, cable installation and offshore dredging. Another important business line is precision stone dumping referred to as subsea rock installation. Tideway currently operates three state-of-the-art fallpipe vessels: the DP2 fallpipe vessels 'Seahorse' (18,500 t), 'Rollingstone' (11,500 t) and the Ice Class vessel 'Flintstone' (20,000 t). In 2018 they expect the delivery of the DP3 MPV 'Living Stone' which will also have subsea rock installation capabilities.

1.2. Problem Definition

The fallpipe vessels of Tideway are equipped with a closed fallpipe system for their rock placement operations. The closed fallpipe system consists of multiple standard sized pipe sections, water inlet sections, an upper pipe section and a lower pipe section that all can easily be mounted on top of each other. On the fallpipe vessels two different systems of connecting the fallpipe to the vessel are in use. On two of the vessels the pipe sections rest on the ROV and the ROV is connected to the ship with steel wires ensuring the suspension of the entire fallpipe. However, on the other vessel the upper pipe section is connected to a hang off module, that has the same working principle as a gimbal, despite the ship motions the fallpipe will remain in a straight vertical position. The lower pipe section is the lowest part of the fallpipe system and fits through the ROV. It consists of two sections that can be adjusted by the ROV which results in a change of the height of this section. The other functions of the ROV are the steering of the fallpipe, monitoring the operations, and acting as a platform to perform surveys.

The water inlet sections are located in the upper part of the fallpipe. The number of water inlet sections that are used depend on the water depth of the rock placement operations. The deeper the rock placement operations the more water inlet sections will be used, up to a maximum of three. The function of these water inlet sections is to avoid the water level in the fallpipe to drop too far, a large drop in water level can result in the collapse of the fallpipe. The water inlet sections have variously sized holes in an annular pattern around the

pipe section. With the use of four rings these holes can either be closed off or left open, thereby providing a measure of control for the water inflow.

The presence of rocks in the water column of the fallpipe increases the density of the mixture in the fallpipe. The difference in density between the mixture in the fallpipe and the density of the surrounding sea-water results in the water level drop that is observed in the fallpipe. To keep this water level drop within acceptable limits the density in the mixture column is lowered with the use of the water inlet sections. In the situation that no water would be added to the system the velocity of the rocks in the fallpipe would be solely dependent on the settling velocity of the rocks. However, there is an inflow of water present resulting in a water current and therefore the velocity of the rocks is dependent on both the settling velocity and the water current.

Put concisely, an increase of the water level drop in the fallpipe is the result of an increase in the mixture density in the fallpipe. To counteract this a higher amount of water inflow is required which results in an increase of the water velocity in the fallpipe that eventually leads to higher outflow velocities of the fallpipe flow.

High outflow velocities of the fallpipe flow can result in unsatisfactory berm shapes and in very extreme cases to a crater like profile of the berm. Furthermore, high outflow velocities which result in high impact velocities could potentially negatively effect subsea structures. To avoid these events from happening the production is limited to a safe quantity, resulting in a lower outflow velocity. Another measure that is used is to increase the stand-off distance (SOD). The stand-off distance is the distance from the exit of the fallpipe to the seabed. A larger SOD will give a greater dispersal of the rocks, hence less accuracy, and will be a less efficient procedure. Since Tideway strives for maximum production neither one of the measures mentioned above are seen as the desired solution.

The production of the fallpipe system is in general dependent on three factors: the outflow velocity, the density of the mixture and the cross-sectional area of the fallpipe exit. An increase of the outflow velocity or density of the mixture will immediately lead to higher outflow velocities. Whereas, increasing the cross-sectional area of the fallpipe exit comes with numerous dimensional constraints. It is however clear that in order to acquire a high production rate all three of the parameters have to be kept as high as possible.

The information set out above resulted in the following problem statement:

High outflow velocities from the closed fallpipe system result in high impact velocities of the rock particles on the seabed, this has negative effects on the berm profile creation and the existing infrastructure.

1.3. Objective

The objective of this thesis is identify a solution to reduce the outflow velocity of a closed fallpipe system in order to reduce the impact velocity of rock particles on the seabed. To achieve this objective a thorough insight into the parameters that influence the outflow velocity of the closed fallpipe system of Tideway is required. Possible measures to reduce this outflow velocity need to be set up and analyzed and eventually will need to result in the selection of one solution. The selected solution has to be able to work while maintaining current production rates. The area of interest for the modelling of the solution will be on the lower end of the fallpipe, see Figure 1.1.

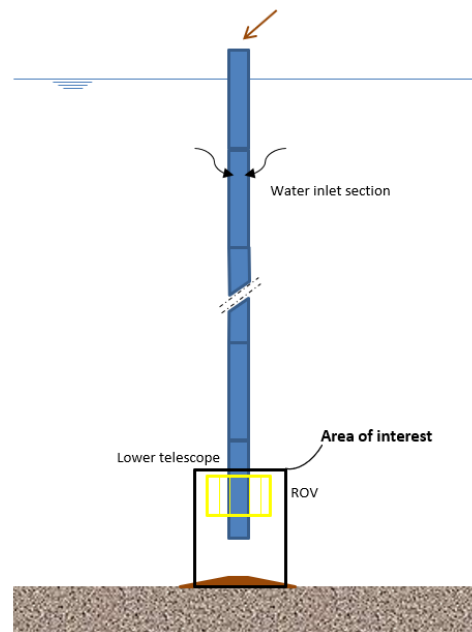


Figure 1.1: Area of interest

The following main research question is set up to achieve the objective described above:

- *How to reduce the impact velocity of rock particles on the seabed exiting the fallpipe while maintaining production rates?*

The main research question is supported by the following sub-questions:

- *Which factors influence the outflow velocity?*
- *What are possible solutions to reduce the impact velocity of the rock particles?*
- *Which one of the proposed solutions is the best option to reduce the impact velocity of rock particles?*
- *What is the effect of the proposed solutions to the fallpipe outflow velocity and therefore the impact velocity of rock particles?*
- *What is the influence of the selected outflow velocity reduction solution to the rock particle settling path below the fallpipe?*

1.4. Approach

The approach to solve the problem described in the problem definition can be split up into different phases. The first phase will be the literature study; the function of this part of the thesis is to get a better understanding of processes that take place in the fallpipe focusing on the processes that affect the outflow velocity. During this phase of the thesis the further insight into the fallpipe processes will be used to come up with a range of solutions to reduce the outflow velocity of the fallpipe. Each of these solutions will be subjected to

a preliminary analysis to assess their viability. With the use of a multi criteria analysis (MCA) one of the proposed outflow reduction solutions will be selected. This process describes the transfer from the first phase of the thesis to the second phase. The second phase will describe the selected reduction measure in detail and a numerical model describing the area of interest, as shown in Figure 1.1, with and without the reduction measure will be developed. The fluid behaviour in the area of interest will be simulated with the use of a computational fluid dynamics (CFD) model and the output generated by this model will be used as input into the numerical model that will describe the rock particle trajectory in the area of interest with and without the reduction measure. This will result in a complete overview of the effect of the selected reduction measure.

2

Subsea Rock Installation

This chapter will describe for what purpose subsea rock installation is used within the offshore industry. The first section will describe the general installation techniques that are used for the range of environments sub-sea rock installation is applied to. Finally, the system in use by Tideway Offshore Solutions will be introduced, the system that currently is installed and operated on the fallpipe vessel 'Flintstone'.

2.1. Areas of Application

Subsea rock installation is widely used within the offshore industry, the main reason being the broad application area. Area's of application include but are not limited to: seabed preparation works, scour protection, pipeline protection, prevention of upheaval- and/or lateral buckling of a pipeline, insulation, providing a separation during crossings of pipelines or cables, mitigation of free span of pipelines, stabilisation and offshore ballasting works [IADC, 2012]. Figure 2.1 illustrates some of these area's of application.

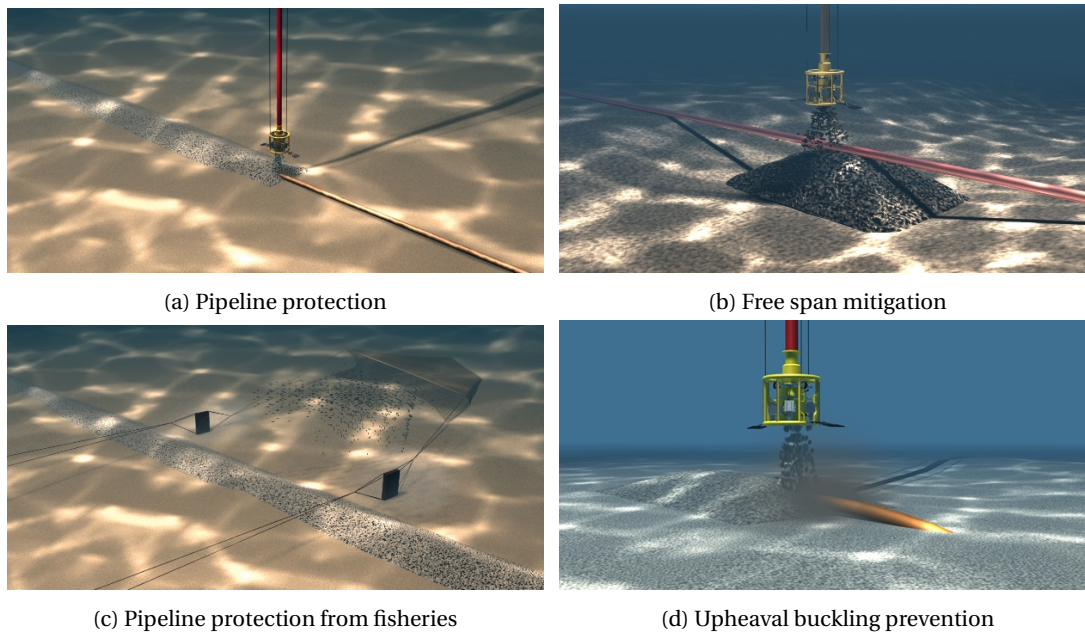


Figure 2.1: Area's of application [Tideway Internal Images]

The four main techniques that are used for subsea rock installation are: side-stone dumping, bottom door dumping by means of a split hopper barge, installation with the use of a fallpipe and dragline dumping. All four main techniques are displayed in Figure 2.2. The most commonly used techniques are side-stone dumping and fallpipe rock installation. A side-stone dumping vessel is basically a vessel with a flat deck

where rock is loaded onto, where by means of hydraulic- or mechanical “bulldozer blades” the rock is pushed over the side of the vessel into the sea. This type of installation is used primarily in shallow water depths up to 50 metres. In deeper water depths it becomes very hard to ensure placement accuracy due to influences from currents. This is the reason that for subsea rock installation in water depths ranging from 50 metres up to 2000 metres a fallpipe system is used. Two different types of fallpipe systems can be distinguished: the closed fallpipe system and the flexible fallpipe system. The latter consist series of bottomless plastic buckets that are being hold together with two chains. The closed fallpipe system is build up out of multiple pipeline sections that are connected to each other. In most cases at the lower end of both of the fallpipe systems a remotely operated vehicle (ROV) is attached. The ROV is used for steering of the fallpipe, survey operations and monitoring of the rock installation operation.

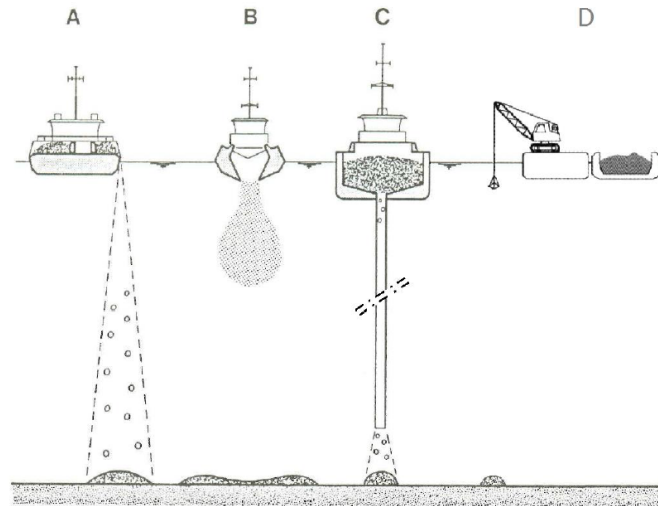


Figure 2.2: A) Side-stone dumping vessel, B) Split hopper barge, C) Fallpipe vessel, D) Dragline
[Kevelam]

2.2. Tideway's 'Flintstone' Rock Placement Vessel

CONFIDENTIAL

3

Rock Properties

This chapter will shortly describe the different types of rock that are available. Furthermore certain characteristics of rock are discussed that are important to consider for subsea rock installation procedures. Finally a description is given of rock gradings that are used in rock placement operations by Tideway.

3.1. Rock Types

Rocks can be divided into three major classes, the division between the classes is made by looking at the formation process of the rock. These three major classes are: igneous rock, sedimentary rock and metamorphic rock. [Carmichael]

Igneous rock is formed by solidified magma. They are formed at high temperatures and originate from deep within the Earth. The two most familiar igneous rock types are granite and basalt. Granite is a hard and tough rock type and has been in use throughout human history for a wide range of applications. Basalt is mainly used for construction projects.

Sedimentary rocks are formed by sedimentation, accumulation and compaction of the settled material at the surface of the earth. The sediment is formed by the weathering of other rocks. The most commonly known types of sedimentary rock are sandstone and limestone.

Metamorphic rocks are formed under the influence of high temperature, high pressure and chemical processes on pre-existing rocks. Formation of metamorphic rocks can simply happen by with rocks situated deep beneath the earth's surface by presence of high temperatures and high pressures of the above situated layers. Well known metamorphic rocks are schist and marble.

3.2. Rock Mass and Size

The rock mass can easily be determined by means of simply weighing the rock material. However determining the diameter of the rock is a more difficult task due to the irregular shape of rocks. The larger in size the stones get the harder it becomes to perform a sieve test to get the median diameter (D_{50}), therefore the median diameter is replaced by the median nominal diameter (D_{n50}) for larger stones [Verhagen and Jansen, 2014]. This gives the the following relationship between the median mass (M_{50}) and median nominal diameter of the rock [CIRIA; CUR; CETMEF, 2007]:

$$D_{n50} = \left(\frac{M_{50}}{\rho_s} \right)^{\frac{1}{3}} \quad (3.1)$$

In literature a relation is given between the median nominal diameter and the median diameter [CIRIA; CUR; CETMEF, 2007] [Verhagen and Jansen, 2014] [Laan, 1996]:

$$D_{n50} = \sqrt[3]{F_s} \cdot D_{50} \quad (3.2)$$

The conversion constant of F_s referred by as the shape factor has a value of $F_s \cong 0.60$, this gives for $\sqrt[3]{F_s} = \sqrt[3]{0.6} = 0.84$. The shape factor is experimentally determined by Laan, G.J. and based on several different rock types and gradings. As a result of this shape factor it is now possible to set-up a relation between the median diameter, median nominal diameter and the median mass by combining Eq. 3.1 and Eq. 3.2:

$$F_s = \left(\frac{M_{50}}{\rho_s D_{50}^3} \right) \cong 0.60 \quad (3.3)$$

The background information describing this value of the shape factor is missing, since the report describing it by Laan, G.J. published in 1981 has gone missing. The value itself can however be found in later publications by Laan, G.J. [Laan, 1982] [Laan, 1996] and in The Rock Manual [CIRIA; CUR; CETMEF, 2007]. Since the background information on the value of the shape factor is missing [Wittman, 2015] performed research on it. He derived a new value of 0.86 which differs very little from the value of Laan, G.J. which is $\sqrt[3]{F_s} = \sqrt[3]{0.6} = 0.84$. Therefore [Wittman, 2015] recommendation is to use his newly derived 0.86 value, since for this value a theoretical justification is available.

3.3. Rock Shape

The shear strength, permeability and filtering properties of core- and underlying rock layers is an indirect result of the rock shape. Two uncorrelated shape descriptors are available these are the length-to-thickness ratio (LT) and the blockiness (BLc), describing the form and compactness respectively. The form and compactness affect the packing density, layer thickness, ease of construction and hydraulic stability in rock placement. These two shape descriptors are described in The Rock Manual [CIRIA; CUR; CETMEF, 2007] as follows:

Length-to-thickness ratio: the maximum length of the rock (l) divided by the minimum distance between two parallel lines where the rock would just pass through (t). It is important to note that high LT-ratios increase the possibility of blockage of the fallpipe.

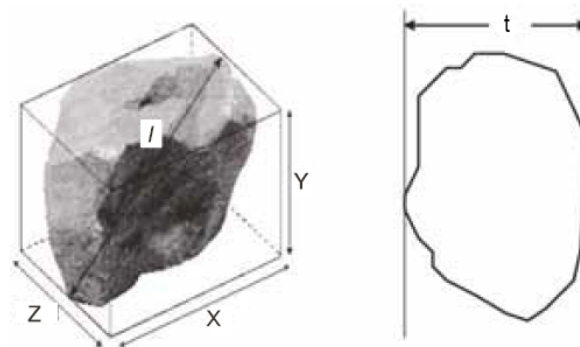


Figure 3.1: LT ratio measurement [CIRIA; CUR; CETMEF, 2007]

Blockiness: is the rock volume divided by the volume of an orthogonal box with minimum volume that encloses the rock. This can be expressed as follows:

$$BLc = \left(\frac{M}{\rho_s} \cdot \frac{1}{X \cdot Y \cdot Z} \right) \cdot 100 \quad (3.4)$$

Where X, Y and Z describe the three sides of the orthogonal box.

Finally, depending on the origin of the rock material there are two other characteristics that are used to describe the rock material: roundness and proportion of crushed or broken surfaces. In order to determine whether adequate mechanical interlocking of the rocks takes place these two characteristics are considered.

3.4. Rock Grading

The rock used in subsea rock installation is in most cases obtained from a quarry. The rock sample that is obtained from this quarry will contain rocks with a variety of different weights and sizes. Therefore the uniformity of the sampled rock can be described with the rock grading width. The three main grading widths that can be distinguished are: narrow or single-sized grading, wide grading and very wide or quarry run gradation. In Table 3.1 the three main grading widths are given, where D_{xx} and W_{xx} are the percentage of total mass smaller or lighter than a given size or weight, respectively. [CIRIA; CUR; CETMEF, 2007]

Table 3.1: The three main grading widths [CIRIA; CUR; CETMEF, 2007]

Grading width	D_{85}/D_{15}	W_{85}/W_{15}
Narrow or single-sized grading	Less than 1.5	1.7 - 2.7
Wide grading	1.5 - 2.5	2.7 - 16
Very wide or quarry run grading	2.5 - 5.0	16 - 125+

European standards however define gradings in terms of lower and upper sieve sizes, for example the following grading category: $G_C85/15$ means “Grading: Coarse with 85 % of the aggregate passing the upper sieve class (size) and 15 % of the aggregate passing the lower sieve class (size)”. However it is stated that these grading categories are actually there as assistance and the supplier and purchaser of the rock material can use a different grading upon agreement of both parties. [Technical Committee CEN/TC 154 “Aggregates”, 2013]

The rock gradings used by Tideway for the majority of its subsea rock placement projects are the following: the 1 - 3 inch, the 1 - 5 inch, the 1 - 8 inch and the CP90/250 grading. The details of these gradings are displayed in Table 3.2.

Table 3.2: Grading classes used by Tideway [Internal Information Tideway]

Grading class 1 - 3 inch							Grading class 1 - 8 inch						
$D_{\#}$	[%]	5	50	90	0	0	$D_{\#}$	[%]	10	30	50	70	90
min	[mm]	16	40	60	0	0	min	[mm]	16	45	90	115	130
max	[mm]	32	60	90	0	0	max	[mm]	32	90	120	150	180

Grading class 1 - 5 inch							Grading class CP90/250						
$D_{\#}$	[%]	5	50	90	0	0	$D_{\#}$	[%]	5	15	50	90	98
min	[mm]	16	60	110	0	0	min	[mm]	45	90	125	-	-
max	[mm]	32	90	135	0	0	max	[mm]	-	-	-	250	360

4

Rock Installation

4.1. Single Rock Installation

When a single rock particle is dropped in liquid it will settle as a result of the gravity force that is acting on the rock particle. The rock particle accelerates as it moves downward until the resistance of the drag force from the liquid acting on the particle equals the gravitational force of the particle. At this point in time the rock particle will reach its terminal or equilibrium settling velocity. In most literature reference is made to this velocity as either terminal settling velocity (v_{ts}) or equilibrium settling velocity (v_e). [Miedema, 2015]

The three forces that are needed to compute the equilibrium settling velocity are: the gravity force, buoyancy force and drag force of the rock particle. With the use of Newton's Second Law we get the following:

$$F_D - F_b + F_g = M \cdot \frac{dv_e}{dt} \quad (4.1)$$

Where F_D the particle drag, F_b the particle buoyancy and F_g the particle gravitational force are computed by:

$$F_D = C_D \frac{1}{2} \rho_w |v_w - v_e| (v_w - v_e) A_p \quad (4.2)$$

$$F_b = \rho_w g V_p \quad (4.3)$$

$$F_g = \rho_s g V_p \quad (4.4)$$

Where C_D is the drag coefficient of the particle, v_e is the particle velocity, v_w is the velocity of the surrounding water, ρ_w = density of water, A_p = area of particle subjected to flow resistance, g the gravitational constant, V_p = volume of particle and ρ_s = density of particle. Furthermore M consists of the mass of the particle and the added mass. When the rock particle accelerates the surrounding fluid must accelerate as well this is modeled as the added mass. The added mass for a spherical particle is calculated by [Spurk and Aksel, 2008]:

$$M_a = \frac{1}{12} \pi d^3 \rho_w \quad (4.5)$$

Where d is the diameter of the particle. This will result in the following equation for stagnant flow ($v_w = 0$), which is also described by [Van Rhee, 2015]:

$$(V_p \rho_s + M_a) \frac{dv_e}{dt} = -A_p C_D \frac{1}{2} \rho_w v_e^2 + V_p g (\rho_s - \rho_w) \quad (4.6)$$

In the case of a stagnant and stationary flow ($\frac{dv_e}{dt} = 0$) and where the specific density is $\Delta = \frac{\rho_s - \rho_w}{\rho_w}$, Equation 4.6 simplifies to the following formula for the terminal settling velocity, or equilibrium settling velocity, of a single particle:

$$v_{ts} = v_e = \sqrt{\frac{2\Delta g V_p}{C_D A_p}} \quad (4.7)$$

In the case of a spherical particle this simplifies to the following equation for the terminal settling velocity of a sphere:

$$v_{ts} = v_e = \sqrt{\frac{4d\Delta g}{3C_D}} \quad (4.8)$$

The rock particles in this thesis are assumed to be spherical. The drag coefficient C_D of a spherical particle is a function of the particle Reynolds number, $Re_p = \frac{v_{ts} \cdot d}{\nu}$, where ν is the kinematic viscosity. The drag coefficient for the laminar (Stokes), transitional and turbulent flow regimes are described by the following formulae in that order [Van Rhee, 2002]:

$$C_D = \begin{cases} \frac{24}{Re_p} & Re_p \leq 1 \\ \frac{24}{Re_p} + \frac{3}{\sqrt{Re_p}} + 0.34 & 1 < Re_p < 2000 \\ 0.4 & Re_p \geq 2000 \end{cases} \quad (4.9)$$

Substituting the C_D relation for laminar flow into Equation 4.8 results in the Stokes equation for terminal settling velocity:

$$v_{ts} = \frac{\Delta g d^2}{18\nu} \quad (4.10)$$

The transition flow regime requires iterations to compute the terminal settling velocity. However, an alternative to the iteration procedure is available for the transitional regime in the form of an empirical relation. The equation set up by 'Ruby and Zanke' is applicable to the transitional regime:

$$v_{ts} = \frac{10\nu}{d} \left(\sqrt{1 + \frac{\Delta g d^3}{100\nu^2}} - 1 \right) \quad (4.11)$$

Finally, in the case of the turbulent flow regime C_D has a constant value resulting in the following equation:

$$v_{ts} = \sqrt{\frac{10\Delta g d}{3}} \quad (4.12)$$

As an alternative to the equations given above one could use the equation published by [Ferguson and Church, 2004] which is applicable to a very wide range:

$$v_{ts} = \frac{\Delta g d^2}{C_1 \cdot \nu + \sqrt{0.75 \cdot C_2 \Delta g d^3}} \quad (4.13)$$

Where the C_1 and C_2 values are 18.0 and 0.4 for smooth spheres, 24.0 and 1.2 for angular natural particles and 18.0 and 1.0 in the case of particles of varied shapes.

4.2. Multiple Rock Installation

Hindered Settling

The settling velocity of rock particles decreases when a large number of rock particles is settling in a confined space. The decreased settling velocity of these rock particles is referred to as the hindered settling velocity v_{hs} . [Richardson and Zaki, 1954] constructed an equation to determine this hindered settling velocity:

$$v_{hs} = v_{ts} \cdot (1 - C)^n \quad (4.14)$$

Where C is the volumetric concentration and n the hindered settling factor. According to [Richardson and Zaki, 1954] the following values for n should be used:

$$\begin{aligned} Re_p < 0.2 & \quad n = 4.65 \\ 0.2 < Re_p < 1.0 & \quad n = 4.35 \cdot Re_p^{-0.03} \\ 1.0 < Re_p < 200 & \quad n = 4.45 \cdot Re_p^{-0.1} \\ Re_p > 200 & \quad n = 2.39 \end{aligned} \quad (4.15)$$

[Rowe, 1987] formulated a convenient way to estimate the hindered settling factor, n :

$$n = \frac{4.7 + 0.41 \cdot Re_p^{0.75}}{1 + 0.175 \cdot Re_p^{0.75}} \quad (4.16)$$

Furthermore [Garside and Al-Dibouni, 1977] published a new relation to compute n that is valid for very high particle Reynolds numbers. Since the particle Reynolds numbers for the rock particles in the fallpipe are of the order 10^4 this relation can also be applied:

$$n = \frac{5.1 + 0.27 \cdot Re_p^{0.9}}{1 + 0.1 \cdot Re_p^{0.9}} \quad (4.17)$$

Rock group settling phases

The settling process of rock groups is described by [van der Wal, 2002] and based on experiments conducted where a group of rock particles is released above a water tank. The five phases identified by [van der Wal, 2002] are:

1. Acceleration of the rock group: Water is entrained and trapped in the rock group, this water can be seen as added mass.
2. Deceleration of the rock group: When the maximum settling velocity of the rock group is reached further entrainment of water in the rock group will and the resulting volume increase of the rock group will lead to deceleration of the rocks.
3. Front of larger rock particles: At a certain point the rock group velocity has decreased to the equilibrium settling velocity of the largest rock particles then the largest rock particles will fall out of the rock group at the front. This process will keep on repeating itself for the subsequent largest rock particles.
4. The rocks fall as individual rocks: The rock group is dispersed thereby limiting the influence of rocks on each others fall velocity.
5. Radial runoff: In the case the rocks reach the seabed before reaching phase 3 there will still be a substantial amount of entrained water present in the rock group. When this water impacts at the seabed it will create a radial flow pattern that can transport rock particles radially.

It is assumed that just before the rock particles exit the fallpipe they have reached phase 4 as described by [van der Wal, 2002], however hindered settling still needs to be taken into account since the fallpipe ensures a confined environment which is not the case for the experiments conducted by [van der Wal, 2002]. It is therefore concluded that the settling velocity of rock particles exiting the fallpipe is described by the equilibrium settling equation, Equation 4.7, and corrected for hindered settling with Equation 4.14.

4.3. Fallpipe Rock Installation

Increasing rock installation depths requires the use of fallpipe systems to ensure placement accuracy for sub-sea rock installation. One can distinguish two main types of fallpipe systems: the flexible fallpipe system and the closed fallpipe system.

4.3.1. Flexible Fallpipe System

In order to compute the rock- and water exit velocities [Beemsterboer, 2013] describes an iterative computation procedure used by Van Oord. The fallpipe system in use at Van Oord is an open (bucket) system in contrary to the closed system in use at Tideway. Therefore, it is not possible to use the parameters of the closed system in the calculation method for the open system as a comparison.

1. Set a starting water velocity v_{water}
2. Calculate the terminal velocity or equilibrium velocity of the individual rocks, the rocks are assumed to be spheres and can therefore be calculated with Equation 4.8, hereafter in this calculation procedure referred to as $v_{equilibrium}$

3. Calculate the exit velocity of the rock water mixture:

$$v_{exit} = v_{equilibrium} + v_{water} \quad (4.18)$$

4. Calculate the rock concentration just under the fallpipe exit:

$$c_m = \frac{\frac{P_r}{\rho_s}}{v_{exit} \cdot A_{min}} \quad (4.19)$$

5. Calculate the mixture density

$$\rho_m = c_m \rho_s + (1 - c_m) \rho_w \quad (4.20)$$

6. Calculate the water velocity by equating the driving and frictional forces in the fallpipe:

$$\Delta p_{driving} = \Delta p_{loss,total} \quad (4.21)$$

$$(\rho_m - \rho_w) g h = \frac{1}{2} (\zeta_{carnot} + \zeta_{wall}) \cdot \rho_m v_{water}^2 \quad (4.22)$$

$$v_{water} = \sqrt{\frac{2(\rho_m - \rho_w) g \cdot L_{eff}}{(\zeta_{carnot} + \zeta_{wall}) \rho_m}} \quad (4.23)$$

7. Return to Step 1 and check if the error between the 'set starting water velocity' and the v_{water} calculated in Step 6 is acceptable, if this is not the case use the newly obtained v_{water} as 'starting water velocity' and repeat the iteration.

In this calculation procedure is v_{water} the water velocity at the end of the fallpipe in [m/s], v_{exit} the velocity of the rock particles at the exit in [m/s], $v_{equilibrium}$ the terminal settling velocity of individual rock particles in [m/s], P_r the production rate in [kg/s], c_v the volumetric concentration, A_{fp} the fallpipe exit cross-sectional area in [m²], $p_{driving}$ and $p_{fric,total}$ the driving and frictional forces in the fallpipe in [Pa], ζ_{carnot} and ζ_{wall} Carnot- and wall the loss coefficients and L_{eff} the effective fallpipe bucket length in [m].

4.3.2. Closed Fallpipe System

CONFIDENTIAL

4.3.3. Impact Assessment

It is important to investigate the impact velocity of the rock particles and the water flow on the seabed or existing infrastructure for fallpipe operations. High impact velocities will negatively affect the berm built up and shape, whereas insufficient berm shapes will require remedials to achieve a satisfying berm shape. The execution of remedials will require extra installation time and rock material all leading to higher costs. Not only the impact velocity is important to consider, but also the impact energy. In the case of subsea rock installation onto existing infrastructure certain limits regarding the impact energy will be set, the impact energy is highly dependent on the impact velocity and will therefore influence the maximum allowable impact velocity. Two common methods to calculate the impact velocity of rock particles onto the seabed or existing infrastructure are discussed.

“Method I”

The impact velocity is calculated with the formula for the terminal settling velocity of a particle, see Equation 4.7, the effect of flow acceleration as a result of the water flow is therefore not taken into account. The area subjected to flow resistance and the volume of the rock particle are calculated as follows:

$$A_{rock} = \left(\sqrt[3]{F_s \cdot d_{max}} \right)^2 \quad (4.24)$$

$$V_{rock} = \left(\sqrt[3]{F_s \cdot d_{max}} \right)^3 \quad (4.25)$$

Where d_{max} is the maximum rock diameter of the selected grading and F_s is rock shape factor as described in Chapter 3.2.

The impact energy as a result of this impact velocity is calculated with the following formula:

$$E_{imp} = \frac{1}{2} (m + m_a) \cdot v_{ts}^2 \quad (4.26)$$

Where E_{imp} is the impact energy in [J], v_{ts} is the terminal settling velocity in [m/s], m is the rock particle mass in [kg] and m_a the added mass in [kg] which can be calculated with Equation 4.5.

In the Table 4.1 the impact velocity and impact energy for the four different rock gradings described in Chapter 3.4 are presented according to the calculation procedure of “Method I”. Since the velocity term is squared in the energy impact calculation a small increase in impact velocity will yield a large increase in impact energy as can be seen in Table 4.1.

Grading Type	[-]	1 - 3 inch	1 - 5 inch	1 - 8 inch	CP90/250
Max. rock size, d_{max}	[mm]	90	135	180	360
Impact velocity, v_{ts}	[m/s]	1.5	1.9	2.2	3.1
Impact energy, E_{imp}	[J]	1.9	9.5	29.9	478.0

Table 4.1: Impact velocity and energy according to “Method I”

“Method II”

The second method that can be used to determine the impact velocity takes into account the effect of flow acceleration as a result of the water flow contrary to the first method. This method is described by [Beemsterboer, 2013], the impact velocity is determined as follows:

$$v_{imp} = \begin{cases} v_{exit} & 0 \leq x \leq x_{ch} \\ \left(\frac{x_{ch}}{x} \cdot v_{water}\right) + v_{equilibrium} & x > x_{ch} \end{cases} \quad (4.27)$$

Where the description and computation of v_{exit} , v_{water} and $v_{equilibrium}$ are given in Chapter 4.3.1 and x_{ch} is the characteristic length for when the flow fully established is, which is $x_{ch} = 6.3 \cdot D_{min}$ according to [Rajaratnam, 1976].

A specific method of calculating the impact energy is not described by [Beemsterboer, 2013]. However, using the impact velocities determined in “Method II” as input in the impact energy relation of “Method I” (see Equation 4.26) will result in higher impact energy values when compared to using “Method I” to calculate the impact velocity.

5

Fallpipe Outflow

This chapter describes the fluid flow below the fallpipe towards the seabed. The continuous supply of rock into the fallpipe results in a water-level drop in the fallpipe that is countered by adding extra water to the fallpipe system by means of water inlet sections as was already explained in Chapter 1. The downward directed flow as a result of the density difference of the mixture inside the fallpipe and the addition of momentum by the water inlet sections results in a downward directed flow of the mixture towards the fallpipe exit. The resulting outflow at the fallpipe exit can therefore be described as a jet flow. In this chapter is the velocity development of this jet flow described with empirical relations. This jet flow is assumed to be in pure water and effects as a result of buoyancy and rocks in the fallpipe flow are neglected. The first section of this chapter will further specify this jet flow and introduces the different jet regions. The remaining sections will give detailed descriptions of the different jet regions and their respective empirical velocity development relations.

Note: in this chapter is the axial direction of the jet flow, or fallpipe represented by 'x' and the axial velocity 'u', the radial direction is represented by 'r' and 'v', respectively

5.1. Circular Turbulent Jet

The outflow is specified further by checking whether the flow is in the laminar or turbulent flow regime. There is no exact number that describes the shift from laminar to turbulent flow. However, flows with a Reynolds number higher than approximately 2000 can be considered turbulent in most cases [Spurk and Aksel, 2008]. The Reynolds number is determined in the same manner as for the particle Reynolds number which is described in Chapter 4, only now it is applied to the flow instead of the particle:

$$Re = \frac{U \cdot L}{\nu} \quad (5.1)$$

Where U is the characteristic velocity in this case the flow velocity in the fallpipe in $[m/s]$, L is the characteristic length in this case the fallpipe diameter in $[m]$ and ν the kinematic viscosity in $[m^2/s]$. The Reynolds number of the fallpipe is in the order of 10^6 and can therefore be considered turbulent. The circular cross-section of the fallpipe as well as the turbulent flow behavior make that the outflow of the fallpipe can be described as a circular turbulent jet.

The circular turbulent jet is impinging on the seabed and can therefore be separated into three distinctive flow regions: the free jet region, the impinging jet region and the wall jet region, see Figure 5.1. [Rajaratnam and Mazurek, 2005] The free jet region can be further divided up into the flow development region and the region of fully developed flow, see Figure 5.1b. [Nobel, 2013] The flow regions will be discussed further in the remaining sections of this chapter.

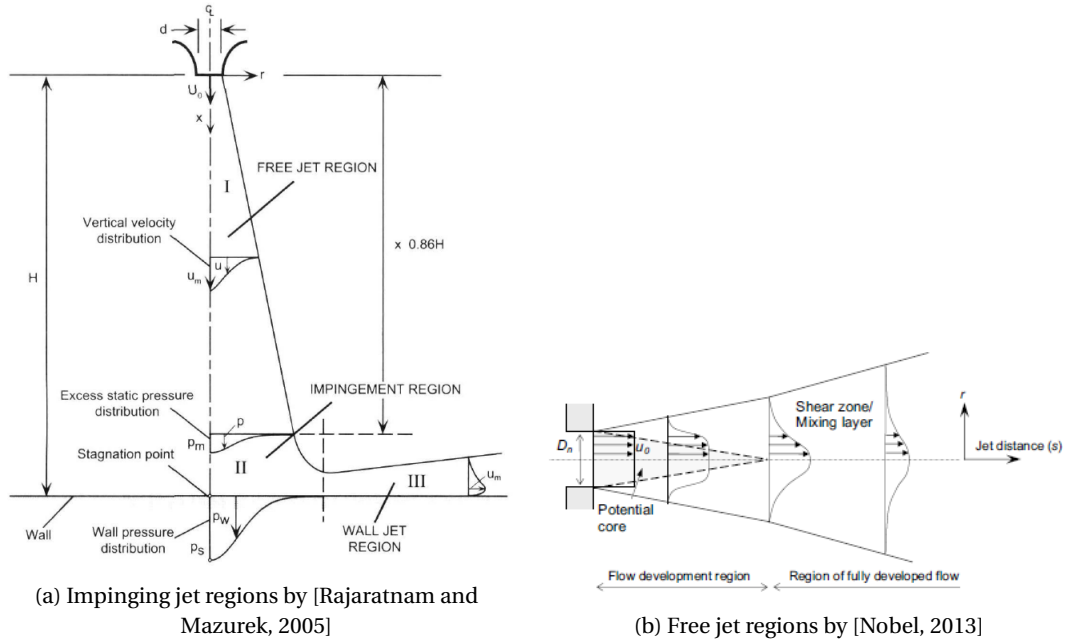


Figure 5.1: Definitions of jet regions

5.2. Free Jet Region

The free jet region consist of the flow development region and the region of fully developed flow. Empirical relations for the free jet region are discussed in this section.

Flow Development Region

It is assumed that the velocity is uniform at the exit of the jet nozzle, or fallpipe exit, for the circular turbulent jet. As a result of the velocity difference between the jet and the surrounding water a mixing shear layer is formed. Transfer of mass and momentum takes place in this mixing layer and the surrounding water is entrained in the jet flow, this process causes the unhindered velocity region of the jet to decrease with increasing distance from the jet nozzle, or fallpipe exit. The region where the velocity remains unhindered is called the potential core, see Figure 5.1b. The flow development region is described as the region where the potential core exist. [Nobel, 2013]

The maximum flow velocity in the free jet region is found at the centerline of the jet flow. In the flow development region is the centerline completely located in the potential core. The maximum velocity of the jet flow in the flow development region is therefore equal to the uniform velocity at the jet nozzle, or fallpipe exit. In literature different potential core lengths are given [Rajaratnam, 1976] describes that for practical purposes a potential core length of $6.3 \frac{x}{D}$ can be used, whereas [Nobel, 2013] uses a potential core length of $6.2 \frac{x}{D}$. [Rajaratnam, 1976] also describes potential core lengths of $7.32 \frac{x}{D}$ and $5.75 \frac{x}{D}$ for the Tollmien-type solution and Goertler-type solution, respectively. The Tollmien-type solution is a velocity distribution for a circular turbulent jet based on the Prandtl mixing length hypothesis, whereas the Goertler-type solution is based on the eddy-viscosity model of Prandtl.

Region of Fully Developed Flow

The flow velocity in the region of fully developed flow will diminish with increasing distance from the jet nozzle, or fallpipe exit. In [Rajaratnam, 1976] a relation is developed for the region of fully developed flow to describe the decay of the maximum velocity, see Equation 5.2:

$$u_m = u_0 \left(\frac{6.3}{\frac{x}{D}} \right) \quad (5.2)$$

The Tollmien-type solution derived by [Rajaratnam, 1976] for the maximum velocity in the region of fully developed flow for a circular turbulent jet is:

$$u_m = u_0 \left(\frac{7.32}{\frac{x}{D}} \right) \quad (5.3)$$

Furthermore, the Goertler-type solution derived by [Rajaratnam, 1976] for the maximum velocity in the region of fully developed flow for a circular turbulent jet is:

$$u_m = u_0 \left(\frac{5.75}{\frac{x}{D}} \right) \quad (5.4)$$

Where in Equations 5.2, 5.3 and 5.4 u_0 is the uniform velocity at the jet nozzle, or fallpipe exit in $[m/s]$ and the $\frac{x}{D}$ is the axial distance measured from the jet nozzle or fallpipe exit to the position of interest in the region of fully developed flow divided by the nozzle diameter, or fallpipe diameter. The result of these equations is the maximum velocity u_m in $[m/s]$ that is located at the centerline of the jet flow. [Nobel, 2013] also describes a relation for u_m as can be seen in Equation 5.5:

$$u_m = \sqrt{\frac{k_1}{2}} u_0 \frac{D}{s} e^{-k_2 \frac{r^2}{s^2}} \quad (5.5)$$

Where D is the nozzle diameter in $[m]$, s the distance from the nozzle in $[m]$, r the radial distance from the centerline in $[m]$ and where k_1 and k_2 are entrainment coefficients, with a value of 77 and 87.3 respectively. With this information the velocity profile at the centerline in the free jet region can be constructed. In Figure 5.2 the normalized centerline velocity for these relations is plotted against the $\frac{x}{D}$.

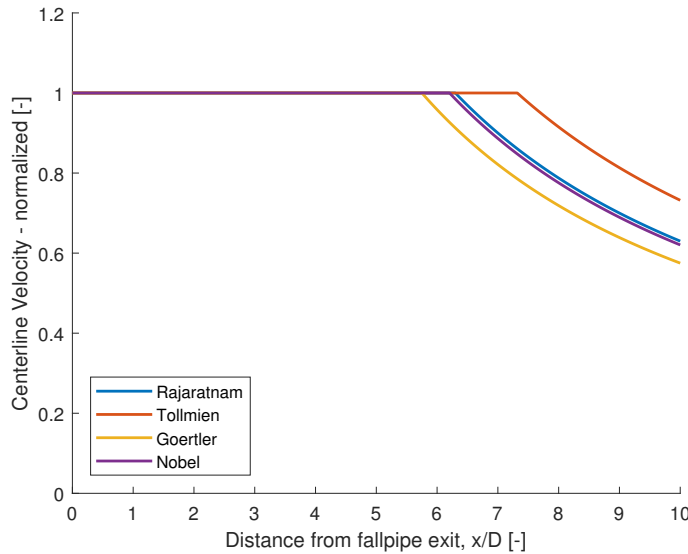


Figure 5.2: Normalized centerline velocity for the free jet region

5.3. Impinging Jet Region

The velocity development in the impinging jet region is dependent on the SOD. The stand-off distance as was explained before is the distance measured from the jet nozzle, or fallpipe exit to the seabed. [Beltaos and Rajaratnam, 1977] distinguishes three different SOD zones: a small SOD zone for $SOD < 5.5D$, a transition zone for approximately $5.5D \leq SOD \leq 8.3D$ and a large SOD zone for $SOD > 8.3D$. The large and small SOD zone maximum velocity profiles are discussed below, it is however worth mentioning that the majority of the subsea rock installation works take place in the large SOD zone. Furthermore, note that the transition zone is not discussed below since no relevant relations can be found in literature regarding this zone.

Large SOD

For the large SOD zone the impinging jet region will start at $\frac{x}{SOD} > 0.86$ from this location on the jet will start to get affected by the presence of the seabed. In [Ravelli, 2012] the following relation for maximum velocity located at the centerline in the impinging jet region is described, obtained from [Beltaos and Rajaratnam, 1974]:

$$\frac{u_m}{u_{mf}} = 3.10\eta_i\sqrt{1-\eta_i} \quad (5.6)$$

Where u_m is the maximum velocity in [m/s], u_{mf} is the corresponding velocity in the case it was a free jet in [m/s] and η_i is $\frac{x}{SOD}$. If the velocity relation for the free jet of [Rajaratnam, 1976] described in Equation 5.2 is used then this will result in the following centerline velocity profile for the impinging jet region, see Figure 5.3:

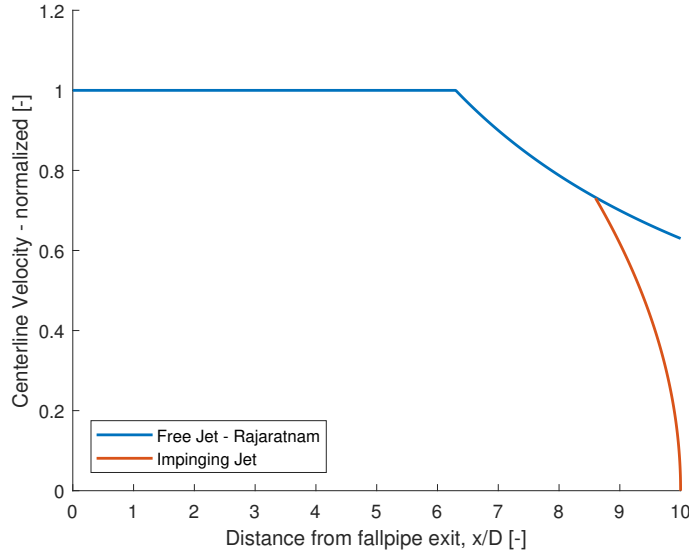


Figure 5.3: Normalized centerline velocity impinging jet region (large SOD)

In the figure above a clear distinction is visible between the free jet velocity profile of a circular turbulent jet and the impinging jet velocity profile which is the case when for example a seabed is present. The transfer from impinging jet region to wall jet region is considered to take place at a radius of $0.22SOD$ from the centerline. [Rajaratnam and Mazurek, 2005]

Small SOD

In the case the SOD is considered small the relation presented above, Equation 5.6, is no longer valid. For the small SOD the impingement region extends to a distance of $1.2D$ measured from the seabed, or wall, upwards towards the jet nozzle, or fallpipe exit, and the radius of the the impinging jet region for a small SOD is $1.4D$ measured from the stagnation point. [Beltaos and Rajaratnam, 1977] developed a relation for the centerline velocity in the impinging jet region for the small SOD zone, see Equation 5.7:

$$u_c = u_0 \left(\frac{\frac{z}{D}}{1.1} \left(2 - \frac{\frac{z}{D}}{1.1} \right) \right) \quad (5.7)$$

Where u_c is the centerline velocity in [m/s], u_0 is the uniform velocity at the jet nozzle, or fallpipe exit in [m/s], z is the distance measured from the seabed, or wall, upwards towards the jet nozzle, or fallpipe exit and D is the nozzle or fallpipe diameter in [m]. The maximum velocity in the impinging jet region for the small SOD zone is not located at the centerline but at a distance r_1 away from the centerline since the region of fully develop flow is not yet reached. The relation between the centerline velocity and the maximum velocity is in this case according to [Beltaos and Rajaratnam, 1977]: $u_m = 1.15 \cdot u_c$. The distance r_1 represents the distance to the inner edge of the annular shear layer and can be calculated with the following relation:

$$r_1 = D \cdot \left(0.50 - 0.069 \frac{SOD}{D} \right) \left(\frac{z}{D} \right)^{-\frac{1}{4}} \quad (5.8)$$

In Figure 5.4 an example is plotted for a SOD of 3D:

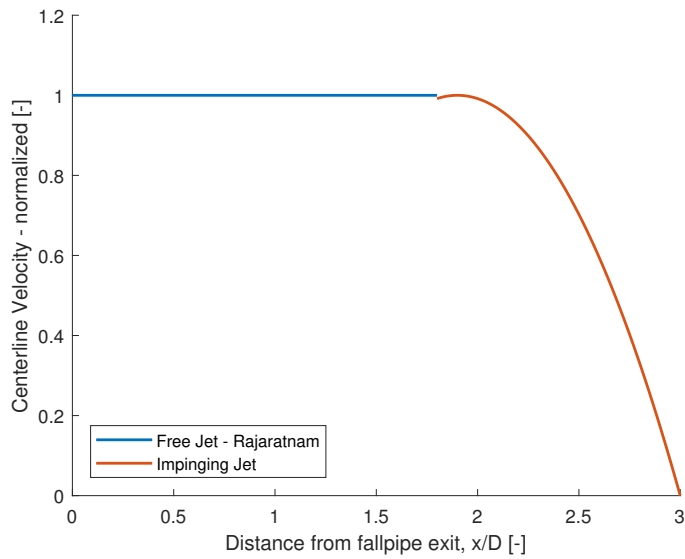


Figure 5.4: Normalized centerline velocity impinging jet region (small SOD)

5.4. Wall Jet Region

It is assumed in this case that the velocity distribution in the wall jet region is distributed axisymmetrically and the relevant velocity to investigate in the wall jet region is the horizontally directed flow velocity. Relations for the small and large SOD zones are discussed below. The transitional SOD zone is not discussed since no relevant relations can be found in literature for this respective zone.

Large SOD

For the large SOD zone [Rajaratnam, 1976] derived the same relation as in Equation 5.11 only the coefficient of C_u is replaced with a value of 1.03, see Equation 5.9. This relation derived by [Rajaratnam, 1976] is based on the experimental results of [Poreh et al., 1967]. It is clear that this relation is also independent of the distance above the wall, or seabed.

$$v_m = u_0 \left(\frac{1.03}{\left(\frac{x}{D}\right)} \right) \quad (5.9)$$

This relation is plotted in Figure 5.5.

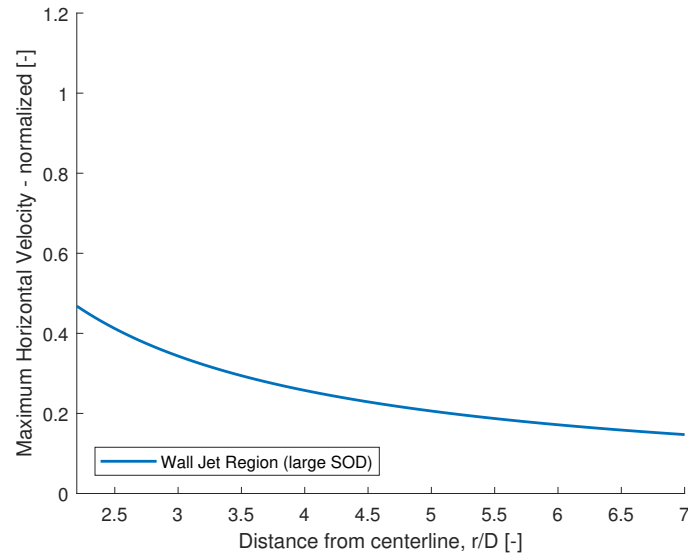


Figure 5.5: Normalized maximum horizontal velocity wall jet region (large SOD)

The maximum horizontal velocity v_m that is obtained with this equation can be used in Equation 5.10 obtained from [Ravelli, 2012] that was adapted from [Verhoff, 1963] to plot the horizontal velocity profile for the wall jet region.

$$v = v_m \left(1.4794\eta^{\frac{1}{2}} (1 - \text{erf}(0.67753\eta)) \right) \quad (5.10)$$

Where $\eta = \frac{z}{b_v}$, $b_v = 0.087 \cdot r$ is the distance in the vertical direction where the horizontal velocity is equal to $v_m/2$, erf is the error function, r the radial distance from the centerline in [m] and z the vertical distance measured from the wall or seabed upwards in [m]. The horizontal velocity profile for the wall jet region is plotted in Figure 5.6. The horizontal velocity for is normalized with the maximum velocity for each radial location.

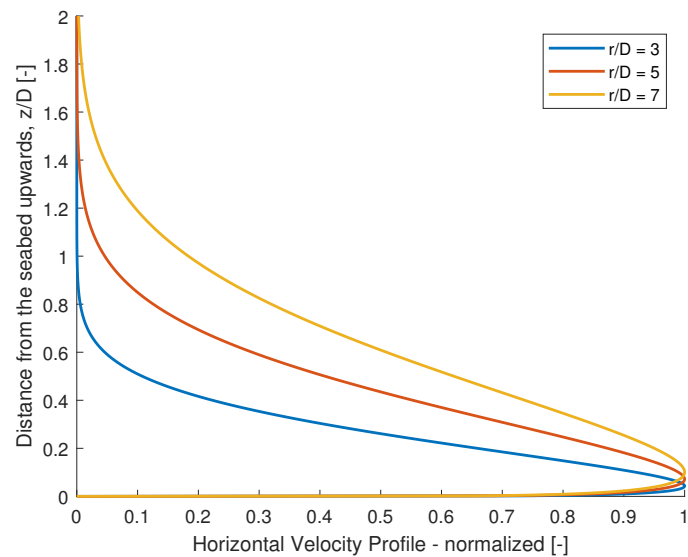


Figure 5.6: Normalized maximum horizontal velocity profile wall jet region (large SOD)

Small SOD

In the case of the small SOD zone [Beltaos and Rajaratnam, 1977] proposes the following equation supported by experimental results of [Hrycak et al., 1970]:

$$v_m = u_0 \left(\frac{C_u}{\frac{r}{D}} \right) \quad (5.11)$$

Where v_m is the maximum horizontal velocity in the wall jet region in $[m/s]$, $C_u \approx 1.0$, r the radial distance measured from the centerline in $[m]$ and D is the diameter of the jet nozzle, or fallpipe exit. [Beltaos and Rajaratnam, 1977] states that the horizontal velocity profile in the wall jet region is independent of the distance above the wall, or seabed. This relation is plotted in Figure 5.7 for a radius r from $1.4D$ until $7D$.

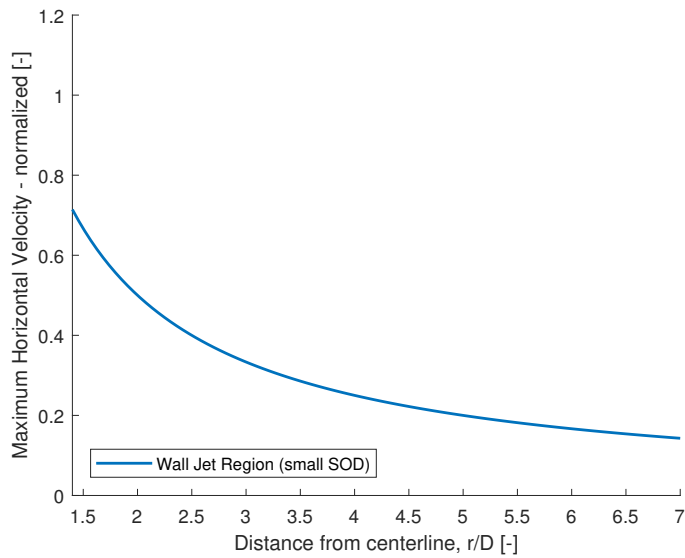


Figure 5.7: Normalized maximum horizontal velocity wall jet region (small SOD)

6

Conceptual Measures to Reduce Fallpipe Outflow Velocities

CONFIDENTIAL

6.1. Concept Generation

CONFIDENTIAL

6.2. Concept Selection

CONFIDENTIAL

6.2.1. Concept Screening

CONFIDENTIAL

6.2.2. Multi Criteria Analysis

CONFIDENTIAL

6.2.3. Result

CONFIDENTIAL

Computational Fluid Dynamics Analysis

This chapter will describe how CFD is utilized to get a better understanding of the fallpipe outflow and the effect of installing a deflector at the fallpipe end. Firstly, the different simulation cases that are tested in ANSYS Fluent will be outlined. Secondly, the main results of the performed mesh independency study are described. Subsequently, the initial- and boundary conditions and turbulence models used in the set-up of the CFD simulations are elaborated. Next, the CFD simulations that represent the current situation of the fallpipe outflow, the impinging jet case, are described and validated. Finally, the CFD simulations of the fallpipe outflow with the use of a deflector are presented.

7.1. Simulation Plan

Prior to setting up the CFD simulations a simulation plan has been set up. The objective of this plan is to determine and list which CFD cases are to be simulated. The main dimensional parameters considered are the SOD, the length and width of the outflow domain and the length of the fallpipe to be modelled. The SOD is chosen to have a minimum of $7.5 \cdot D$ and a maximum of $17.5 \cdot D$ with varying values in between. The minimum and maximum of the SOD are the result of analyzing fallpipe operational data [Internal Information Tideway]. The length and width of the outflow domain are standard set at $15 \cdot D$ to accommodate the radial flow pattern at the seabed. However, in some cases when it was necessary the length and width of the outflow domain are increased to accommodate the flow pattern. The fallpipe length to be modelled is set at $4 \cdot D$. In literature different values are advised to acquire a fully developed velocity profile in turbulent flow, for example: [Lien et al., 2004] advises to use a ratio of $\frac{y}{D} = 130$, Nikuradse [1933] advises a ratio of $\frac{y}{D} = 40$ and [Cengel and Cimbala, 2006] gives a ratio of $\frac{y}{D} = 10$ for pipe flows of practical engineering interest, where y is the fallpipe centerline and D the fallpipe diameter. The longer the fallpipe section of the simulation the higher the amount of computational power and time that is required. Since in this research the focus is on the outflow domain of the fallpipe, the fallpipe section of the simulation is minimized and set at $4 \cdot D$. This value is chosen to give the velocity profile some distance to develop while keeping the required computational power and time for the flow development to a minimum, see Figure 7.1:

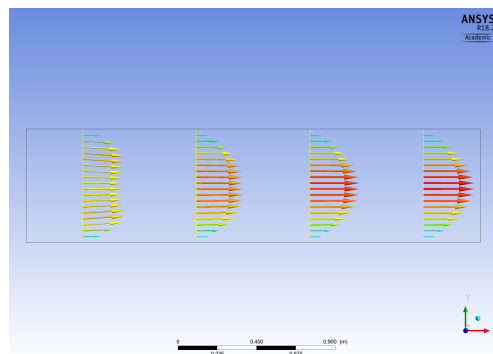


Figure 7.1: Velocity profile development fallpipe length section of $4 \cdot D$

Apart from the dimensional parameters three other main parameters are considered: the input velocity, the turbulence model and the seabed roughness. The input velocities of the fallpipe are varied between 2.5, 5.0 and 7.5 [m/s], where 5.0 [m/s] is representative for the fallpipe velocities of current production rates used by Tideway. Two different turbulence models are used in the simulations the $k - \epsilon$ model and $k - \omega SST$ (Shear-Stress Transport) model. The seabed roughness to be used can be determined from the grain size of the sediment at the seabed. The report of [Rees, H.L., Eggleton, J.D., Rachor, E., Vanden Berghe, 2007] gives the mean grain size of the sediment on the seabed in the North Sea. These values are used as input in the relation suggested by [Soulsby, 1997], $k_s = 2.5 \cdot d_{50}$, which gives the three main k_s parameters of 0.00025, 0.00050 and 0.00100. The k_s values that represent the rock gradings discussed in Chapter 3.4 are also considered, since a part of the rock grading is already on the seabed after the operations have started.

In Appendix E an overview is given of all the main parameters that are varied for every simulation and in Appendix F the results of all the performed simulations are presented.

7.2. Mesh Independency Study

An important part of performing reliable CFD simulations is a mesh independency study. Since computational power and time is limited a sufficiently accurate mesh needs to be generated for the respective problem taking into account these limitations. The purpose of a mesh independency study is to find a mesh accuracy that produces a solutions that will not deviate significantly when the mesh is further refined, thereby ensuring a mesh independent solution for the problem.

The mesh independency study that was carried out resulted in the selection of a tetrahedral mesh with the main parameters as described in Table 7.1.

Table 7.1: Result Mesh Independency Study

	Selected Mesh	
Min Size	0.00045	[m]
Max Face Size	0.045	[m]
Max Tet Size	0.113	[m]
Growth Rate	1.2	[-]

To give the reader an impression of the amount of cells used in the simulation domain with the selected mesh, consider the following:

- An outflow domain with the following dimensions $L = 9.75$ [m] x $W = 9.75$ [m] x $H = 9.75$ [m];
- A fallpipe section of $4 \cdot D$ length and diameter $D = 0.65$ [m];
- Inflation layers are present on the fallpipe wall and the bottom boundary of the outflow domain.

This would result in a mesh of roughly 9.1 million cells when the mesh parameters described in Table 7.1 are used. In Appendix D a more extensive overview of the mesh independency study is presented and more details regarding the inflation layers are described in Appendix D.2.

7.3. Set-up

Fluid flows can be described by partial differential equations (PDE) and most of these PDE's cannot be solved analytically. To solve these CFD is used, where the set of methodologies that facilitate a computer to provide us with a numerical simulation of fluid flows is CFD as we know it today. [Hirsch, 2007] The program of choice to perform the CFD simulations is as mentioned earlier ANSYS Fluent, to be more specific ANSYS Fluent v18.2. The simulation is set up in a complete 3-dimensional domain with the mesh parameters as described in the previous section.

Initial Conditions

In order to perform the CFD simulations in Fluent the user has to set up certain initial conditions. Fluent uses the initial conditions that you put in as an initial guess. Properly setting up the initial conditions that

you provide Fluent with will lead to a decrease in computational time to reach a solution. The turbulence intensity is the first value to set up:

$$I = 0.16 \cdot (Re_{D_H})^{-1/8} \quad (7.1)$$

Where Re_{D_H} is the Reynolds number based on the hydraulic diameter, D_H , of the fallpipe. The hydraulic diameter is equal to the fallpipe diameter since the fallpipe has a circular cross-section, so $D_H = D = 0.65$ [m]. With the turbulence intensity computed and the inlet velocity known the turbulent kinetic energy can be calculated:

$$k = \frac{3}{2} (u_{avg} \cdot I)^2 \quad (7.2)$$

The turbulence length scale for fully developed pipe flow can be determined as well:

$$l = 0.07 \cdot L \quad (7.3)$$

Where L is the diameter of the fallpipe. The computed turbulent kinetic energy and turbulence length scale are used as input in the equations to determine either the turbulent dissipation rate or the specific turbulence dissipation rate, depending on the turbulence model that is used:

$$\varepsilon = C_\mu^{\frac{3}{4}} \frac{k^{\frac{3}{2}}}{l} \quad (7.4)$$

$$\omega = \frac{k^{\frac{1}{2}}}{C_\mu^{\frac{1}{4}} l} \quad (7.5)$$

Where C_μ is a dimensionless constant.

The equations just listed to determine the initial conditions are obtained from [ANSYS, 2018b]. It is however not necessary to compute all these values when setting up the CFD model. Fluent only requires you to enter the turbulence intensity and hydraulic diameter these combined with the input velocity give Fluent enough information to determine the remaining initial conditions by itself. It is however important to check whether no mistakes were made in entering these values or if Fluent in the respective set up calculates them differently. Therefore, the initial conditions are computed analytically and compared to the values computed by Fluent.

Boundary Conditions

There are three different boundary conditions that are applied to the boundaries in the Fluent simulation. These boundary conditions are the following [ANSYS, 2018b] [ANSYS, 2018a]:

- *Pressure outlet boundary condition*: this boundary condition is applied to all the outer boundaries of the domain that in practise would represent the surrounding sea. By applying a gauge pressure of 0 in the pressure-outlet panel, a zero pressure gradient at the pressure outlet boundaries will be set. In the case that backflow still occurs at the pressure outlet boundaries, the backflow pressure specification is set for total pressure. This will result in a static pressure that is smaller than the gauge pressure and therefore it stimulates flow out of the domain.
- *Velocity inlet boundary condition*: this boundary condition is applied at the top of the fallpipe section. In this boundary condition you define the flow velocity and initial direction of the flow.
- *Wall boundary condition*: this boundary condition is applied to the fallpipe wall, the seabed and on the deflector for the deflector case simulations. On the wall boundary condition is the no-slip condition applied, so the velocity relative to the wall goes to zero. In the wall boundary condition it is possible to adjust the roughness height of the wall, which was previously described in the first section of this chapter as k_s .

Turbulence Models

To determine which turbulence models to use for the CFD simulations, comparable CFD simulations were investigated in literature. [Mossad and Deo, 2015] concluded that for the numerical modelling of the velocity field of a plane jet flow good results were obtained for the standard $k - \varepsilon$ turbulence model and the $k - \omega SST$ model showed the best performance. [Arabnejad et al., 2016] concluded from its CFD simulation of round

impinging jets that the $k - \omega$ and RSM model performed better than the $k - \varepsilon$ but no model was superior, since no model performed better than the others for all conditions and locations. The $k - \varepsilon$ model is a very well know turbulence model. It is widely researched and used in engineering applications and the research listed above for similar CFD simulations showed no reasons to not use this turbulence model, and therefore will it be used as turbulence model in the CFD simulations. The $k - \omega SST$ model is another popular turbulence model which combines the $k - \omega$ and $k - \varepsilon$ turbulence models. It can use the $k - \omega$ model in the inner region and switches to the $k - \varepsilon$ model for free flow region. These properties of the $k - \omega SST$ model combined with its good results in comparable literature are the reason that this model will be used as well. To conclude, the CFD simulations in this thesis will be performed with the $k - \varepsilon$ and $k - \omega SST$ turbulence models. The chosen turbulence models are explained below.

The $k - \varepsilon$ turbulence model:

The turbulent kinetic energy k and its rate of dissipation ε can be obtained from the transport equations set-up by [Launder and Spalding, 1974]:

$$\frac{\partial}{\partial t}(\rho k) + \frac{\partial}{\partial x_i}(\rho k u_i) = \frac{\partial}{\partial x_j} \left[\left(\mu + \frac{\mu_t}{\sigma_k} \right) \frac{\partial k}{\partial x_j} \right] + G_k - \rho \varepsilon \quad (7.6)$$

$$\frac{\partial}{\partial t}(\rho \varepsilon) + \frac{\partial}{\partial x_i}(\rho \varepsilon u_i) = \frac{\partial}{\partial x_j} \left[\left(\mu + \frac{\mu_t}{\sigma_\varepsilon} \right) \frac{\partial \varepsilon}{\partial x_j} \right] + C_{1\varepsilon} \frac{\varepsilon}{k} G_k - C_{2\varepsilon} \rho \frac{\varepsilon^2}{k} \quad (7.7)$$

Where G_k is the generation of turbulent kinetic energy due to mean velocity gradients. Furthermore, by combining k and ε the turbulent viscosity (eddy viscosity) can be determined [Launder and Spalding, 1974]:

$$\mu_t = \rho C_\mu \frac{k^2}{\varepsilon} \quad (7.8)$$

The model constants used for the $k - \varepsilon$ turbulence model in Fluent are as follows:

Table 7.2: Model constants for the $k - \varepsilon$ turbulence model

Model Constant	Value
$C_{1\varepsilon}$	1.44
$C_{2\varepsilon}$	1.92
C_μ	0.09
σ_k	1.0
σ_ε	1.0

The $k - \varepsilon$ model is as mentioned above a well known and tested turbulence model in the industry and it provides the user with reasonable accuracy for a very broad range of applications. Furthermore, it has good convergence and low memory requirements. [ANSYS, 2018a] [Pope, 2000] A known disadvantage of this model is the build up of turbulent kinetic energy near stagnation points which has to be taken into account [Stanford University, 2004]. This can be fixed by potentially using a production limiter. However, for the simulations performed in this thesis with the $k - \varepsilon$ turbulence model the production limiters are not enabled in Fluent.

The $k - \omega SST$ turbulence model:

The $k - \omega SST$ model is an adaption of the $k - \omega$ model by Wilcox [Menter, 1994]. The turbulent kinetic energy k and the specific rate of dissipation ω of the $k - \omega SST$ model can be obtained from the transport equation set up by [Menter, 1994] [ANSYS, 2018a]:

$$\frac{\partial}{\partial t}(\rho k) + \frac{\partial}{\partial x_i}(\rho k u_i) = \frac{\partial}{\partial x_j} \left[\left(\mu + \sigma_k \mu_t \right) \frac{\partial k}{\partial x_j} \right] - \beta^* \rho \omega k + G_k \quad (7.9)$$

$$\frac{\partial}{\partial t}(\rho \omega) + \frac{\partial}{\partial x_i}(\rho \omega u_i) = \frac{\partial}{\partial x_j} \left[\left(\mu + \sigma_\omega \mu_t \right) \frac{\partial \omega}{\partial x_j} \right] - \beta \rho \omega^2 + 2\rho(1 - F_1) \sigma_{\omega 2} \frac{1}{\omega} \frac{\partial k}{\partial x_j} \frac{\partial \omega}{\partial x_j} + G_\omega \quad (7.10)$$

In which G_ω is:

$$G_\omega = \alpha \frac{\omega}{k} G_k \quad (7.11)$$

However, for high Reynolds numbers which is the case α becomes α_∞^* .

The $k - \omega$ SST model is a hybrid model which uses the $k - \omega$ formulation in the near wall region and the $k - \epsilon$ model is activated in the outer region and free shear layers. The switch between these models is made possible by the blending function, F_1 , which is zero near the wall and one in the outer part of the boundary layer and free shear layers. The blending function is defined as follows:

$$\phi = F_1 \phi_1 + (1 - F_1) \phi_2 \quad (7.12)$$

Where the eddy viscosity is modified to account for the transport of turbulent shear stress:

$$\mu_t = \frac{\rho k}{\omega} \frac{1}{\max\left[\frac{1}{\alpha}, \frac{SF_2}{\alpha_1 \omega}\right]} \quad (7.13)$$

And the F_2 is determined by:

$$F_2 = \tanh\left(\left(\max\left[2\frac{\sqrt{k}}{0.09\omega y}, \frac{500\mu}{\rho y^2 \omega}\right]\right)^2\right) \quad (7.14)$$

With y as the distance to the next surface and S is the strain rate magnitude. The model constants used in Fluent for the $k - \omega$ SST turbulence model and its respective blending functions are as follows:

Table 7.3: Model constants for the $k - \omega$ SST turbulence model

Model Constant	Value	Model Constant	Value
α_∞^*	1	$\sigma_{k,1}$	1.176
α_∞	0.52	$\sigma_{\omega,1}$	2.0
α_0	$\frac{1}{9}$	$\sigma_{k,2}$	1.0
β_∞^*	0.09	$\sigma_{\omega,2}$	1.168
R_β	8	α_1	0.31
R_k	6	$\beta_{i,1}$	0.075
R_ω	2.95	$\beta_{i,2}$	0.0828
ζ^*	1.5		
M_{t0}	0.25		

The $k - \omega$ SST model uses the best of two turbulence models in one hybrid model. This hybrid behaviour makes the model suitable to approximate the flow behaviour close to the wall as well as in regions further away from the wall. The blending function's dependency on the distance from the wall makes it less suitable for free shear flows and this could lead to errors. [FLUENT, 2006] Furthermore, limiters in the model prevent the strong build up of turbulent kinetic energy as is the case in the $k - \epsilon$ model. [Bardina et al., 1997] In the $k - \omega$ SST turbulence model simulations in this thesis the 'Production Limiter' is enabled in Fluent since this is standard for ω based turbulence models. The production term of turbulent kinetic energy is limited with the following formulation [ANSYS, 2018a]:

$$G_k = \min(G_k, C_{lim} \rho \epsilon) \quad (7.15)$$

Where the coefficient C_{lim} has a default value of 10. Build up of turbulent kinetic energy in stagnation points is avoided by using this limiter.

7.4. Impinging Jet

This section will describe the results obtained from the CFD simulations for the impinging jet model. The impinging jet model is representative for the fluid flow behaviour of the fallpipe in the current set up. The first variable that was varied throughout the different simulations is the input velocity. Since the expected input velocity of 5 [m/s] can deviate in practice and simulating every possible input velocity is unreasonable the

dependency on the input velocity on the simulated flow velocities is checked. Simulations are performed with the $k - \varepsilon$ turbulence model for two different input velocities and two different SODs. The velocity magnitude at the centerline is normalized for the respective input velocity and plotted in Figure 7.2:

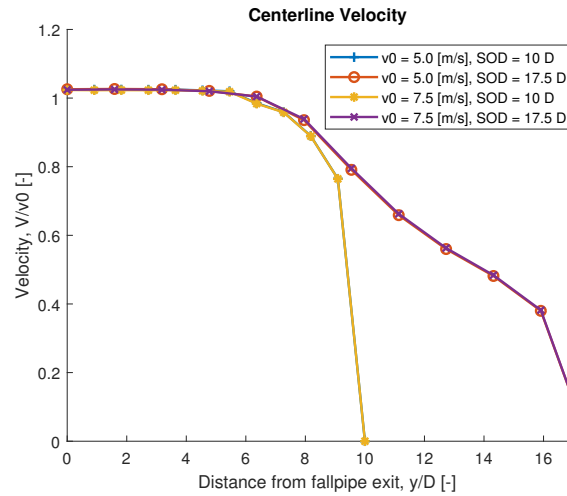


Figure 7.2: Normalized centerline velocities for different input velocities and SOD

The same comparison of simulations is performed with the $k - \varepsilon$ turbulence model for two different input velocities and two different SODs are also plotted for the radial velocity. These results for two different radial positions are plotted in the Figure 7.3, where $0.5D$ and $2D$ are the radial distance measured from the centerline of the impinging jet.

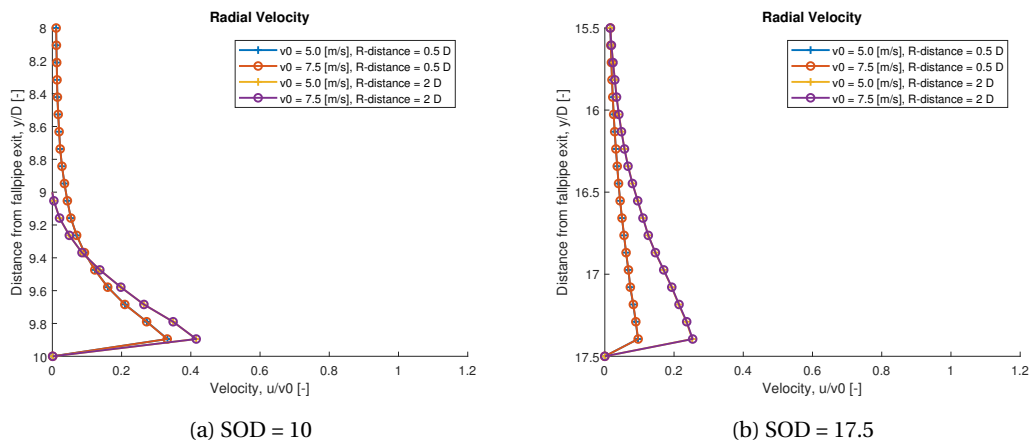


Figure 7.3: Normalized radial velocities for different input velocities and radial location

It can be concluded from these results in Figure 7.2 and 7.3 that the velocity field is completely dependent on the input velocity. Normalizing the velocity field with the respective input velocity will give the same normalized velocity field for different input velocities. Therefore, a normalized velocity field can be used to represent all the possible input velocities. Furthermore, it is clear from Figure 7.2 and 7.3 that the dependency on the input velocity of the velocity field is not disturbed by changes in SOD. The result of this outcome justifies using only 5 m/s as input velocity in the succeeding simulations, as long as the results are normalized so that they can be applied to every input velocity.

In Chapter 7.1 and Appendix E a wide range of values for the roughness height, k_s , to be applied to the seabed boundary are given. The roughness height of the seabed will have the greatest effect on the radial velocity at the seabed. To investigate the influence of the roughness height, simulations are performed for two different

values of k_s at two different SODs with the $k-\epsilon$ model. The resulting normalized radial velocities at two radial locations measured from the centerline at $0.5D$ and $2D$ respectively are plotted in Figure 7.4.

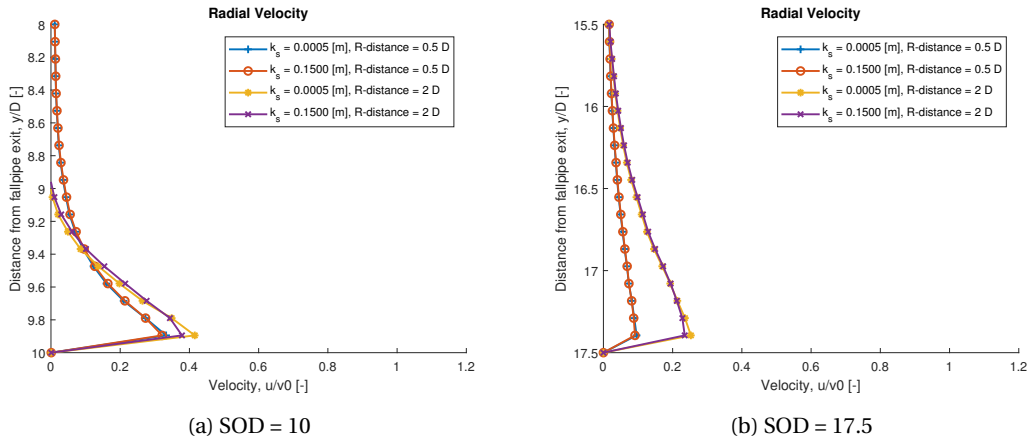


Figure 7.4: Normalized radial velocities for different k_s values and radial location

The result for an increase in roughness height is as expected, the radial velocity close to the seabed shows a higher decrease in velocity when moving from the centerline outwards. However, it is clear from Figure 7.4 that only a very small decrease in radial velocity is noticed for an increase of roughness height from $k_s = 0.0005$ [m] to $k_s = 0.15$ [m] which is a factor of 300. Since the effect of the roughness height of the seabed is so extremely low a constant value of $k_s = 0.0005$ [m] will be used for the succeeding simulations, this value represents the mean k_s value for the North Sea seabed [Rees, H.L., Eggleton, J.D., Racher, E., Vanden Berghe, 2007].

The velocity profiles for the two chosen turbulence models are compared to each other as well. In Figure 7.5 the normalized centerline velocity of the $k-\epsilon$ and $k-\omega$ SST model are compared for two different SODs and in Figure 7.6 the same comparison is made for the normalized radial velocity. Figure 7.5 shows a shorter potential core length of the $k-\omega$ SST model in comparison to the $k-\epsilon$ model. The turbulence models show a roughly similar gradient of the curve after the potential core indicating that their rate of velocity decay is roughly equal in the fully developed flow region.

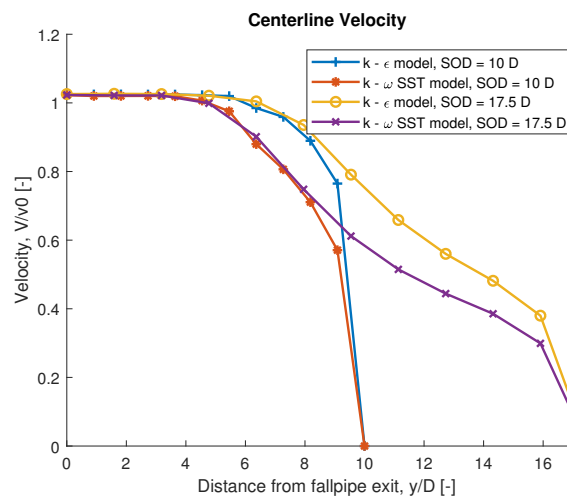


Figure 7.5: Normalized centerline velocities for different turbulence models and SOD

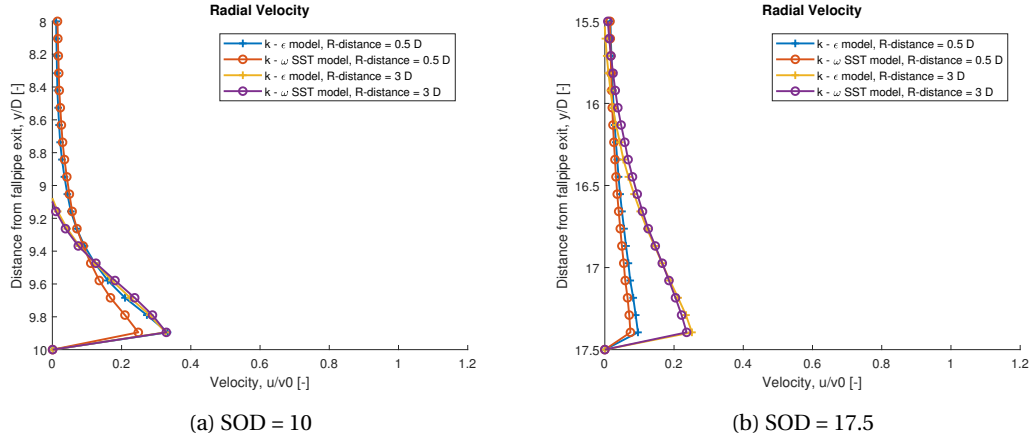


Figure 7.6: Normalized radial velocities for different turbulence models and radial location

In Figure 7.6 it is shown that the radial velocity of the $k-\epsilon$ model is slightly higher than the radial velocity of the $k-\omega$ SST model in the impingement region of the flow as well as the wall jet region of the flow (which starts at around $x/SOD = 0.22$ according to [Rajaratnam and Mazurek, 2005]). However, in the area above the wall jet region the $k-\omega$ SST shows slightly higher radial velocities in comparison to the $k-\epsilon$ model for a SOD of 17.5. A contour plot of the velocity fields is available in Appendix F.

In Chapter 7.3 it is described that for the $k-\epsilon$ model turbulent kinetic energy build up at stagnation points can occur where this is prevented in the $k-\omega$ SST model by the use of limiters. In Figure 7.7 and 7.8 it is shown that the $k-\epsilon$ model experiences build up of the turbulent kinetic energy around the stagnation point, which is the centerline of the jet impinging into the seabed. Furthermore, it is clear that the build up of turbulent kinetic energy around the stagnation point decreases for increasing SOD. The higher amount of turbulent kinetic energy that is build up around the stagnation point is even more clearly visible in Figure 7.9a. However, further away from the stagnation point the turbulent kinetic energy that is created is slightly higher for the $k-\omega$ SST model when compared to the $k-\epsilon$ model as is shown in Figure 7.9b.

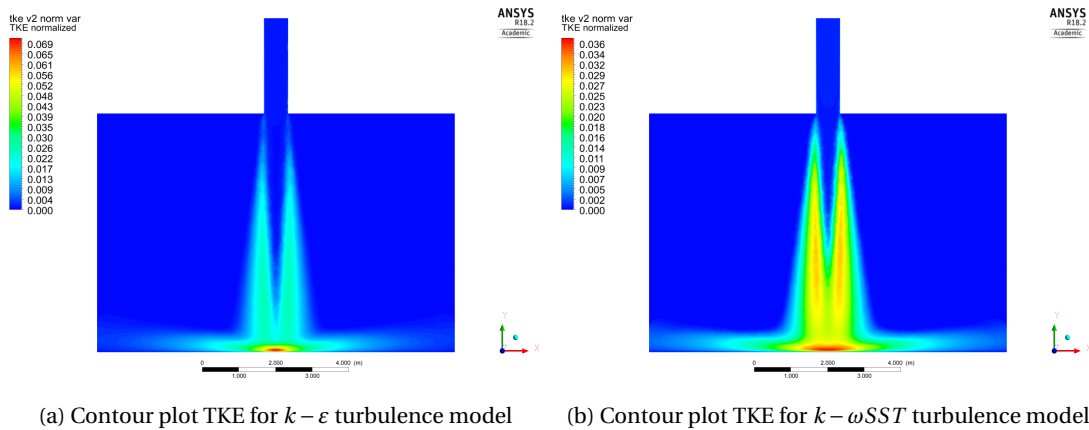
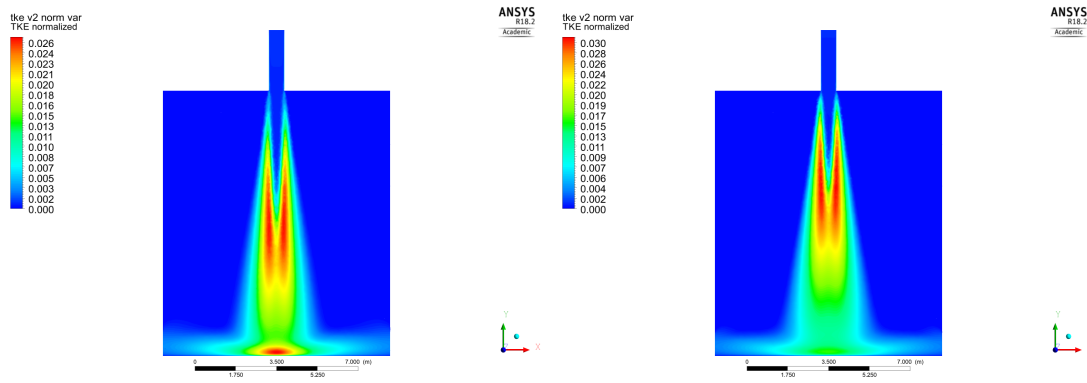
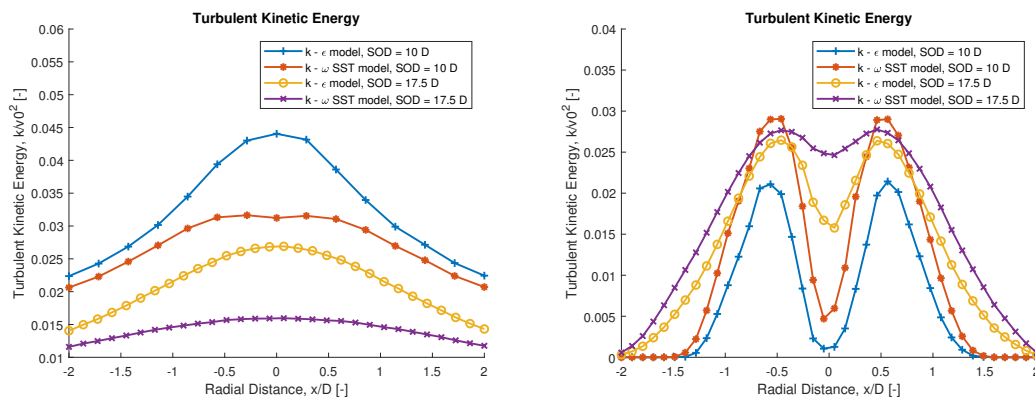


Figure 7.7: Contour plots TKE for different turbulence models with SOD = 10 D



(a) Contour plot TKE for $k - \epsilon$ turbulence model (b) Contour plot TKE for $k - \omega$ SST turbulence model

Figure 7.8: Contour plots TKE for different turbulence models with SOD = 17.5



(a) Distance from the seabed $\frac{1}{4}$ D

(b) Distance from the seabed $\frac{1}{2}$ SOD

Figure 7.9: Turbulent kinetic energy for different turbulence models and location in the flow field

The plots of all the performed impinging jet simulations can be found in Appendix F.

7.4.1. Impinging Jet - Validation

In literature empirical relations are described regarding impinging jets. Validation of the impinging jet case is therefore possible by comparing velocity values at certain jet regions. By validating the CFD results from the impinging jet case with these empirical relations the CFD results are considered to represent an accurate representation of the situation. This section will describe the validation of the CFD results of the impinging jet case with the empirical impinging jet flow equations as described in Chapter 5. First, the free jet region will be discussed followed by the impinging jet region and concluded by the wall jet region.

Free Jet Region

The free jet region is compared for the two turbulence models that were simulated the $k - \epsilon$ and $k - \omega$ SST model, respectively. In Chapter 5 four different relations were given to calculate the centerline velocity in the free jet region. The comparison between these four empirical relations and the CFD results of the two turbulence models is shown in Figure 7.10:

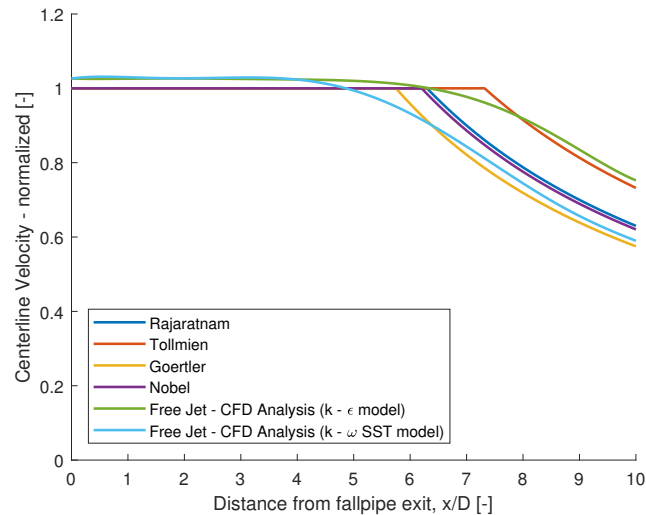


Figure 7.10: Normalized centerline velocity comparison for the free jet region

In Chapter 7.4 it was already shown that the $k - \omega SST$ model showed a shorter potential core length than the $k - \epsilon$ model. Therefore, it is obvious that the $k - \omega SST$ model CFD results are better represented by the empirical relations of Nobel, Goertler and Rajaratnam. Whereas, the Tollmien relation showed a longer potential core length and thereby better matches the CFD results of the $k - \epsilon$ model. It can therefore be concluded from these results, in Figure 7.10, that the CFD results for the free jet region match the empirical relations quite well.

Impinging Jet Region

In Chapter 5 relations for large and small SOD are described, however subsea rock installation works take place in the large SOD zone. Therefore, only CFD results for large SODs are generated in Chapter 7.4 and these are compared to the relation set up by [Beltaos and Rajaratnam, 1974] described in Chapter 5 to validate the solution. Since the $k - \omega SST$ model has a shorter potential core length compared to the $k - \epsilon$ model and for the empirical relation the velocity decrease starts earlier than for the $k - \epsilon$ model, the empirical relation falls in between both turbulence models. However, all three curves show roughly the same velocity decrease after their potential core ends. Figure 7.11 shows that the CFD results for the impinging jet region match the empirical relation very well and this solution is considered validated.

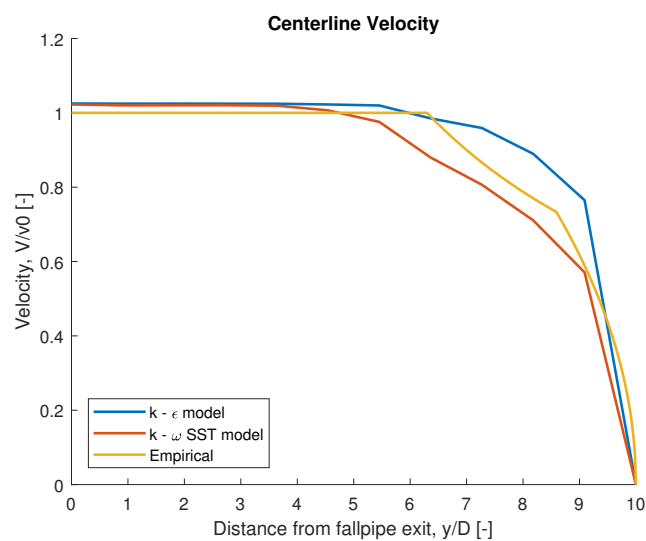


Figure 7.11: Normalized centerline velocity comparison for the impinging jet

Wall Jet Region

Similar to the impinging jet region empirical relations are described for the large and small SOD zone, see Chapter 5. However, the focus of subsea rock installation works is the large SOD zone and therefore the empirical relations for the large SOD zone are compared to the CFD results for the $k-\varepsilon$ and $k-\omega SST$ turbulence models. In Figure 7.12 the $k-\varepsilon$ model is compared to the empirical relation and in Figure 7.13 the $k-\omega SST$ model is compared to the empirical relation. In both figures the horizontal velocity profile in the wall jet region is compared at three different radial locations measured from the centerline: $r/D = 3$, $r/D = 5$ and $r/D = 7$. The horizontal velocity profile at every radial location is normalized by the respective maximum horizontal velocity of that radial location. In Figure 7.12 it is shown that when moving further away from the seabed or when getting closer to the centerline the difference between the empirical relation and the CFD results become bigger. It can be concluded that the $k-\varepsilon$ model CFD results match the empirical relation quite well. For the $k-\omega SST$ model described in Figure 7.13 it is clear that the same observations can be made as for $k-\varepsilon$ comparison to the empirical relation. Further away from the seabed or the closer to the centerline the difference between the $k-\omega SST$ model and the empirical relation becomes bigger. However, it can still be concluded that the CFD results of the $k-\omega SST$ model match the empirical relation quite well. When comparing the two turbulence models it can be seen that the $k-\omega SST$ model matches the empirical relation better closer to the seabed, whereas the $k-\varepsilon$ model is a better match with the empirical relation further away from the seabed.

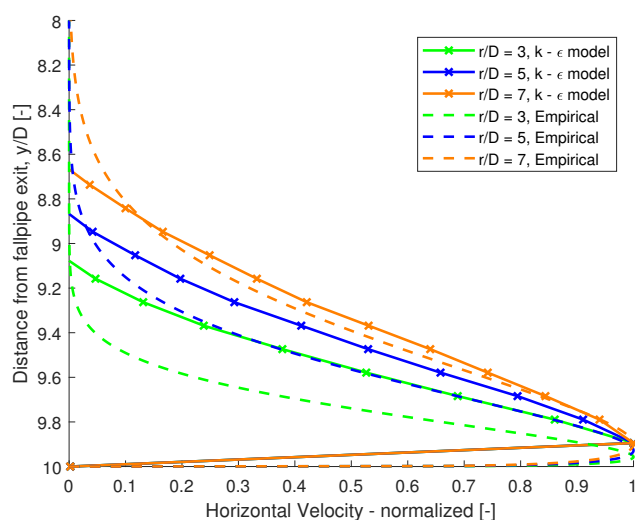


Figure 7.12: Normalized horizontal velocity comparison for the wall jet region, SOD = 10, $k-\varepsilon$ model

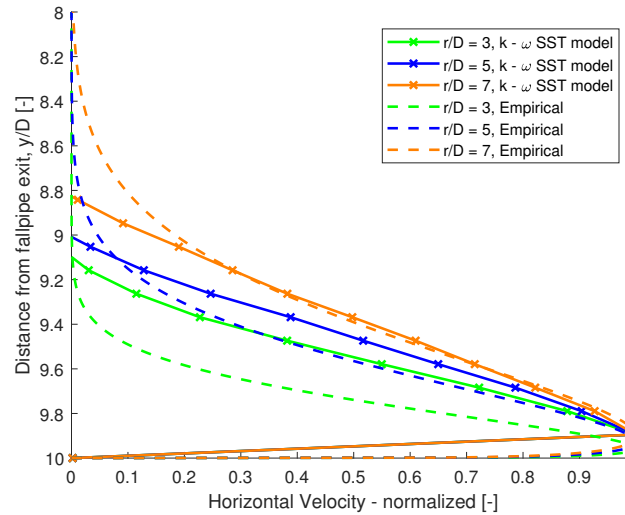


Figure 7.13: Normalized horizontal velocity comparison for the wall jet region, $SOD = 10$, $k - \omega SST$ model

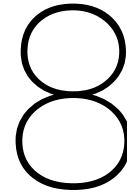
Finally, one can conclude that the comparisons for the free jet region, impinging jet region and wall jet region show good resemblance between the empirical relations and the CFD results for all regions and are therefore considered to be validated. The CFD deflector case described in Chapter 7.5 is an extension of the impinging jet case and is therefore also considered to give an accurate representation of the modelled situation since the impinging jet case is validated.

7.5. Deflector

CONFIDENTIAL

7.6. Conclusion & Results

CONFIDENTIAL



Rock Trajectory Model

In this chapter the rock trajectory model is described that is used to track the rock particles leaving the fallpipe. The rock trajectory model is produced in MATLAB and can describe the rock particle trajectory in the current fallpipe situation, the impinging jet, and the situation for when a deflector is used. In the first section the input and the structure of the MATLAB model is discussed and in the section following the input and model structure the output generated by the model is represented.

Note: in the MATLAB model is the vertical flow from the fallpipe directed towards the seabed defined as the positive direction 'y' and the vertical velocity component is 'v', the horizontal components are represented by 'x' and 'u', respectively

8.1. Input & Model Structure

Data Import

The first step is to import the CFD data from Fluent into MATLAB. The simulation results in Fluent are opened in CFD-Post the post processor of ANSYS for CFD simulations. A plane is generated to get the relevant information for the MATLAB model. The plane contains the CFD results of the respective simulations in an unstructured grid. For MATLAB to import the data in an acceptable time span it is necessary to transform the unstructured grid in CFD-Post to a structured grid with points containing all the necessary information for the MATLAB model. When this transformation is finished the relevant data is exported to .csv-file.

The next step is the importing the .csv-file into MATLAB. This is followed by setting up a grid in MATLAB that is represented by a matrix structure, the structured grid of CFD-Post is then mapped onto the MATLAB grid after which it can be used in MATLAB. This concludes the data import section of the MATLAB model.

Input Parameters & Pre-allocation

The section of the MATLAB model sets some initial input parameters and performs pre-allocation to reduce the computational time of the model. The following values are initialized:

- Number of rocks to use in the model;
- Start time of the model and the time step;
- The fallpipe length, diameter and radius;
- The gravitational constant;
- The fluid density, rock density and specific density (Δ);
- The kinematic viscosity;
- C_μ , the same constant as was used in Chapter 7.3;
- C_L , a constant used to compute the integral time scale used in the Discrete Random Walk Model;
- The drag coefficient of the rock particles;

- The minimum and maximum diameter of the rock size to be used, depending on the chosen grading that is used for the specific model run, the minimum and maximum diameter are used to determine a mean value for the rock grading and a standard deviation;
- The volumetric concentration C and the factor n to compute the hindered settling velocity;

Finally, to conclude this section of the model the locations of the cells that represent the deflector in the matrix structure are determined. If the impinging jet case is modelled, so without a deflector present, then obviously this part of the code is left out.

Main Loop

It starts by setting the loop for the number of rock initialized. Then the first calculations follow, which start with the generation of random rock diameters (assumed to be d_{50}) from a normal distribution set by the initialized mean and standard deviation. This is followed by calculating the mass of every rock particle given below, which is also described by Equation 3.3:

$$M_{50} = F_s^{*3} \cdot rho_s \cdot D_{50}^3 = 0.86^3 \cdot rho_s \cdot D_{50}^3 \quad (8.1)$$

Where $F_s^* = F_s^{\frac{1}{3}} = 0.86$.

The next step is calculating the median normal rock diameter (D_{n50}). The larger in size the stones get the harder it becomes to perform a sieve test to get the median diameter (D_{50}), therefore the median diameter is replaced by the median normal diameter (D_{n50}) for larger stones, as explained in Chapter 3, see Equation 3.1:

$$D_{n50} = \left(\frac{M_{50}}{\rho_s} \right)^{\frac{1}{3}} \quad (8.2)$$

Note that in the MATLAB model D_{n50} is hereafter referred to as $d(i)$. The next step is calculating the settling velocity and hindered settling velocity of the rock particles. The settling velocity is determined with the formula below, which is the same as Equation 4.8, only written differently:

$$v_s = \sqrt{\frac{4\Delta g d}{3 \cdot C_D}} \quad (8.3)$$

This velocity is then used as input into the hindered settling equation which is the same as Equation 4.14, only written differently:

$$v_{hs} = v_e (1 - C)^n \quad (8.4)$$

In the MATLAB model the values of v_{hs} are then stored in v_s so that it is possible to use the notation of v_s in the rest of the program. This is followed by the calculation of the rock particle mass and added mass (see Equation 4.5 for the respective rock particle:

$$(m + m_a) = \frac{\pi}{6} d^3 \rho_s + \frac{\pi}{12} d^3 \rho_f \quad (8.5)$$

Finally the particle relaxation time is determined to be used in the Discrete Random Walk Model later. Particle relaxation time according to [Greimann, 2001]:

$$t_p = \frac{v_s \rho_s \Phi_f^v}{g(\rho_s - \rho_f)} \quad (8.6)$$

Where Φ_f is the fluid volumetric concentration, v is the coefficient that accounts for effects due to particle crowding [Di Felice, 1994] and it is assumed to have a constant value of 1.7 [He and Simonin, 1993].

The following phase of this part of the MATLAB model is determining the start location, or release location, of the rock particles. The start location of the rock particles is determined by setting a minimum and maximum bound which represent the sides of the fallpipe minus half of the rock particle diameter, to make sure the rock particles do not end up outside the fallpipe or on the fallpipe edge. Now that the bounds are determined the rock particle is released on a random location in between these bounds. In the MATLAB model there is the opportunity to disable this release location procedure and to choose for release locations that represent

a normal distribution with the same bounds as for the random location procedure.

Now that the basic parameters are set, the initial fluid velocity (the u- and v direction) are retrieved from the CFD-Post data matrix and the vertical downward rock particle velocity is determined by:

$$v_s = v_f + v_s \quad (8.7)$$

Where v_f is the fluid velocity from CFD-Post. Furthermore, the rock particle velocity in horizontal direction is initialized to be $u_s = 0$ and lift forces on the rock particle are neglected.

Now the first nested for loop in the main loop starts. For a pre-set number of locations is the new location of the rock particle determined. To determine the new rock particle velocity in the next location in the outflow domain the equations of motions for the rock particles are used:

$$(m + m_a) \frac{du_s}{dt} = \frac{1}{8} \pi d^2 C_D \rho_f |\vec{V}| (\bar{u}_f - u_s) \quad (8.8)$$

$$(m + m_a) \frac{dv_s}{dt} = \frac{1}{8} \pi d^2 C_D \rho_f |\vec{V}| (\bar{v}_f - v_s) + \frac{1}{6} \pi d^3 (\rho_s - \rho_f) g \quad (8.9)$$

With:

$$|\vec{V}| = \sqrt{(v_f - v_s)^2 + (u_f - u_s)^2} \quad (8.10)$$

In order to use them in the MATLAB model they are discretized, which gives:

$$u_s^{n+1} = \left(\frac{1}{8} \pi d^2 C_D \rho_f |\vec{V}| (\bar{u}_f - u_s) \right) \cdot \frac{\Delta t}{(m + m_a)} + u_s^n \quad (8.11)$$

$$v_s^{n+1} = \left(\frac{1}{8} \pi d^2 C_D \rho_f |\vec{V}| (\bar{v}_f - v_s) + \frac{1}{6} \pi d^3 (\rho_s - \rho_f) g \right) \cdot \frac{\Delta t}{(m + m_a)} + v_s^n \quad (8.12)$$

With:

- n = current time step
- $n + 1$ = next time step
- Δt = time step

Then the new x- and y positions are computed as follows:

$$x_s^{n+1} = u_s^{n+1} \cdot \Delta t + x_s^n \quad (8.13)$$

$$y_s^{n+1} = v_s^{n+1} \cdot \Delta t + y_s^n \quad (8.14)$$

The next step in this part of the MATLAB model is to check whether or not the next x- or y- location is on the deflector. This check is performed and when the new x- and y- location match one of the predefined deflector locations the model steps into an if loop located in the nested for loop. In this if loop the angle of incidence to the deflector plate is determined with the velocity components at that location. The angle of reflection is assumed to be equal to the angle of incidence to model the worst case scenario. In order to use the angle of reflection in the matrix of the MATLAB model it is transformed and the angle of reflection is determined with respect to the flow domain (not w.r.t. the deflector plate, which is under an angle itself). With this angle known the new u- and v- velocity components of the reflected rock particle are calculated. When this procedure is done the if loop is finished and the rock particle will go further in the nested for loop. In the case no deflector is used then this module will be turned off in the MATLAB model.

The next step in the nested for loop is the Discrete Random Walk Model. The turbulent dispersion of the rock particles is predicted by using this model. The model is described in [ANSYS, 2018b] and adapted to be implemented in this MATLAB model. The particle trajectory is at the moment predicted by using the mean fluid phase velocity (\bar{u}) and the settling velocity of the particle. To predict the dispersion of the particles a fluctuating velocity (u') is now added to the model.

$$u = \bar{u} + u' \quad (8.15)$$

The generation of this fluctuating velocity is done with the help of the Discrete Random Walk Model. The first parameter that is determined is the integral time scale:

$$T_L = C_L \frac{k}{\epsilon} \quad (8.16)$$

Where C_L which was set earlier is 0.30 for the $k - \epsilon$ model and variants of its, which gives:

$$T_L \approx 0.30 \cdot \frac{k}{\epsilon} \quad (8.17)$$

Note that for the $k - \omega SST$ model, ϵ in Equation 8.16 needs to be replaced by $0.09 \cdot k\omega$. The next step is to determine the characteristic eddy lifetime as a random variation about the characteristic time scale, T_L :

$$\tau_e = -T_L \ln(r) \quad (8.18)$$

Where r is a uniform random number greater than zero and less than one and T_L is determined by Equation 8.16.

The fluid velocities in u- and v-direction at the new x- and y-locations are now retrieved from the CFD-Post data matrix. These velocities are necessary to compute the particle eddy crossing time. First, the eddy length scale is determined by rewriting Equations 7.4 and 7.5 for the turbulence model used, respectively the $k - \epsilon$ model and the $k - \omega SST$ model, which gives:

$$L_e = C_\mu^{\frac{3}{4}} \frac{k^{\frac{3}{2}}}{\epsilon} \quad (8.19)$$

$$L_e = \frac{k^{\frac{1}{2}}}{C_\mu^{\frac{1}{4}} \omega} \quad (8.20)$$

Now that the eddy length scale is determined the particle eddy crossing time is determined with Equation 8.21:

$$t_{cross} = -\tau \ln \left[1 - \left(\frac{L_e}{\tau |u - u_p|} \right) \right] \quad (8.21)$$

Now a check is performed which one is smaller the eddy lifetime or the eddy crossing time. For the smallest value of the two the rock particle is assumed to interact with the fluid phase eddy. In the case this smallest time value is reached a new instantaneous velocity is obtained by the following equations:

$$u' = \zeta \sqrt{u'^2} \quad (8.22)$$

$$v' = \zeta \sqrt{v'^2} \quad (8.23)$$

$$w' = \zeta \sqrt{w'^2} \quad (8.24)$$

Where ζ is a normally distributed random number, and:

$$\sqrt{u'^2} = \sqrt{v'^2} = \sqrt{w'^2} = \sqrt{\frac{2k}{3}} \quad (8.25)$$

This instantaneous velocity is added to the fluid velocity in the discretized equations of motions to compute the rock particle velocities for the next step and then the nested for loop repeats itself again until it reaches the set number of steps. The MATLAB model is then concluded by several plotting commands to generate the required output.

8.2. Output

CONFIDENTIAL

8.3. Velocity Magnitude Tracking

CONFIDENTIAL

8.4. Conclusion & Results

CONFIDENTIAL

9

Conclusion & Recommendations

Conclusion
CONFIDENTIAL

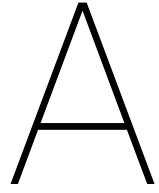
Recommendations
CONFIDENTIAL

Bibliography

- ANSYS,Inc. *ANSYS 18.2 Fluent Theory Guide*. 2018a.
- ANSYS,Inc. *ANSYS 18.2 Flunt User's Guide*. 2018b.
- Arabnejad,H, Mansouri,A, Shirazi,S A, and Mclaury,B S. CFD Simulation of Round Impinging Jet and Comparison with Experimental Data. *Proceedings of the ASME 2016 Fluids Engineering Division Summer Meeting*, (July):1–10, 2016. doi: 10.1115/FEDSM2016-7889.
- Bardina,J E, Field,Moffett, Huang,P G, Coakley,T J, and Aeronautics,National. Turbulence Modeling Validation, Testing, and Development. *NASA Technical Memorandum*, (April), 1997. URL <http://www.ewp.rpi.edu/hartford/{~}ferraj7/ET/Other/References/nasa{~}techmemo{~}110446.pdf>.
- Beemsterboer,T.N. Modelling the immediate penetration of rock particles in soft clay during subsea rock installation, using a flexible fallpipe vessel. Technical report, 2013.
- Beltaos,S. and Rajaratnam,N. Impingement of Axisymmetric Developing Jets. *Journal of Hydraulic Research*, 15(4):311–326, 1977. ISSN 00221686. doi: 10.1080/00221687709499637.
- Beltaos,Spynos and Rajaratnam,N. *Impinging Circular Turbulent Jets*, volume 100. oct 1974.
- Carmichael,Robert S. rock | geology | Britannica.com. URL <https://www.britannica.com/science/rock-geology>.
- Cengel,Yunus A and Cimbala,John M. *Fluid mechanics : fundamentals and applications*. McGraw Hill,, New York :, third edit edition, 2006.
- CFD-online,. Y plus wall distance estimation, 2011. URL <https://www.cfd-online.com/Wiki/Y{~}plus{~}wall{~}distance{~}estimation>.
- CIRIA; CUR; CETMEF,. *The Rock Manual. The use of rock in hydraulic engineering (2nd edition)*. C683, CIRIA, London, 2007.
- Di Felice,R. The voidage function for fluid-particle interaction systems. *International Journal of Multiphase Flow*, 20(1):153–159, feb 1994. ISSN 0301-9322. doi: 10.1016/0301-9322(94)90011-6. URL <https://www.sciencedirect.com/science/article/pii/0301932294900116>.
- Ferguson,R.I. and Church,M. A Simple Universal Equation for Grain Settling Velocity. *Journal of Sedimentary Research*, 74(6):933–937, 2004. ISSN 1527-1404. doi: 10.1306/051204740933. URL <http://jsedres.sepmonline.org/cgi/doi/10.1306/051204740933>.
- Ferziger,Joel H. and Peric,Milovan. *Computational Methods for Fluid Dynamics*. 2002. ISBN 3540420746. doi: 10.1016/S0898-1221(03)90046-0.
- FLUENT,Inc. Modeling Turbulent Flows. Technical report, 2006. URL <http://aerojet.engr.ucdavis.edu/fluenthelp/html/ug/node988.htm>.
- Garside,John and Al-Dibouni,Maan R. Velocity-Voidage Relationships for Fluidization and Sedimentation in Solid-Liquid Systems. *Industrial & Engineering Chemistry Process Design and Development TA -*, 16(2): 206–214, 1977. ISSN 0196-4305.
- Greimann,Blair P. Two-Phase Flow Analysis of Concentration Profiles, 2001.
- He,J and Simonin,Olivier. *Non-equilibrium prediction of the particle-phase stress tensor in vertical pneumatic conveying*, volume 166. jan 1993.

- Hirsch, Charles. *Numerical Computation of Internal and External Flows - Fundamentals of Computational Fluid Dynamics*. Elsevier Butterworth-Heinemann, Amsterdam ;, 2nd ed. edition, 2007. ISBN 9781615835287 1615835288 9780080550022 0080550029.
- Hrycak, P, W. Gauntner, J, T. Lee, D, and N. B. Livingood, J. "Experimental Flow Characteristics of a Single Turbulent Jet Impinging on a Flat Plate". apr 1970.
- IADC,. Facts About Subsea Rock Installation, An Information Update From the IADC, 2012.
- Kevelam, M.D.J. Hydrodynamics below a closed fallpipe system. Technical report, Delft University of Technology.
- Laan, G.J. Kwaliteit en kwaliteitscontrole van breuksteen voor de waterbouw. Technical report, Rijkswaterstaat, Wegbouwkundige Dienst, 1982.
- Laan, G.J. De relatie tussen eisen aan loskorrelige steenmaterialen en ontwerpparameters. Informatie ten behoeve van waterbouwkundige constructies. Technical report, Ministerie van Verkeer en Waterstaat, 1996.
- Lauder, B.E. and Spalding, D.B. The Numerical Computation of Turbulent Flows. *Computer Methods in Applied Mechanics and Engineering*, 3:269–289, 1974.
- Lien, K., Monty, Jp, Chong, Ms, and Ooi, A. The entrance length for fully developed turbulent channel flow. *15th Australasian Fluid Mechanics Conference (Sydney, Australia)*, (December):1–4, 2004. URL <http://www.aeromech.usyd.edu.au/15afmc/proceedings/papers/AFMC00093.pdf>.
- Menter, F. R. Two-equation eddy-viscosity turbulence models for engineering applications. *AIAA Journal*, 32 (8):1598–1605, 1994. ISSN 0001-1452. doi: 10.2514/3.12149. URL <http://arc.aiaa.org/doi/10.2514/3.12149>.
- Miedema, dr.ir. S.A. *OE4607 Introduction Dredging Engineering*. 2015. ISBN 9789461865366.
- Mossad, R. and Deo, R. Numerical Modelling of the Velocity Field of a Plane Jet Flow At Moderate Jet Exit Reynolds Numbers. *11th International Conference on CFD in the Minerals and Process Industries*, (December):1–6, 2015.
- Nikuradse, J. Laws of Flow in Rough Pipes - Translation of "Stromungsgesetze in rauhen Rohren". Technical Report 4, 1933. URL <http://link.aip.org/link/JAPIAU/v14/i8/p399/s1{&}Agg=doi>.
- Nobel, A J. *On the excavation process of a moving vertical jet in cohesive soil*. PhD thesis, 2013.
- Pope, Stephen B. Turbulent Flows. *Journal of Turbulence*, 1:771, 2000. ISSN 1468-5248. doi: 10.1088/0957-0233/12/11/705.
- Poreh, M, Tsuei, Y G, and Cermak, J E. Investigation of a Turbulent Radial Wall Jet. *Journal of Applied Mechanics*, 34(2):457–463, jun 1967. ISSN 0021-8936. URL <http://dx.doi.org/10.1115/1.3607705>.
- Rajaratnam, N. *Turbulent jets*, volume 5. 1976. ISBN 9780444413727. doi: 10.1016/S0167-5648(08)70915-8. URL <http://www.sciencedirect.com/science/article/pii/S0167564808709158>.
- Rajaratnam, N. and Mazurek, K.A. Impingement of circular turbulent jets on rough boundaries. *Journal of Hydraulic Research*, 43(6):689–695, 2005. ISSN 0022-1686. doi: 10.1080/00221680509500388. URL <http://www.tandfonline.com/doi/abs/10.1080/00221680509500388>.
- Ravelli, F.D.C. Improving the efficiency of a flexible fallpipe vessel: An experimental study on the spreading of rock in an impinging plane jet. Technical report, 2012.
- Rees, H.L., Eggleton, J.D., Rachor, E., Vanden Berghe, E. Structure and Dynamics of the North Sea Benthos. ICES Cooperative Research Report. Technical report, 2007.
- Richardson, J. F and Zaki, W.N. *Sedimentation and Fluidization: Part I*, volume 32. jan 1954.
- Rowe, P N. A convenient empirical equation for estimation of the Richardson-Zaki exponent. *Chemical Engineering Science TA* -, 42(11):2795–2796, 1987. ISSN 0009-2509.

- Schlichting,H. *Boundary-Layer Theory*. McGraw Hill,, 7 edition, 1979.
- Schlichting,H and Gerstein,K. *Boundary Layer Theory*. 2000. ISBN 9783662529171.
- Soulsby,R L. *Dynamics of marine sands: a manual for practical applications*. 1997. ISBN 978-0-7277-2584-X. doi: 10.1680/doms.25844.
- Spurk,J.H. and Aksel,N. *Fluid Mechanics*. Springer, 2008. ISBN 9783540735366.
- Stanford University,. *Simulation of Turbulent Flows, ME469B: Computational Methods in Fluid Dynamics Using Commercial CFD Codes*. Technical report, 2004.
- Technical Committee CEN/TC 154 "Aggregates",. EN 13242:2013 Aggregates for unbound and hydraulically bound materials for use in civil engineering work and road construction. Technical report, 2013.
- van der Wal,J.R. *Het valgedrag van steengroepen*. PhD thesis, 2002.
- Van Rhee,C. *On the sedimentation process in a trailing suction hopper dredger*. Technical report, 2002.
- Van Rhee,C. *Lecture Notes OE4727*. page 54, 2015.
- Verhagen,H.J. and Jansen,L. *Ratio between stone diameter and nominal diameter*. Technical report, 2014.
- Verhoff,A. *The Two-Dimensional, Turbulent Wall Jet With and Without an External Free Stream*. Technical report, 1963.
- Witteman,D. *The shape factor of quarry rock. Reassessment of the value and study into parameters of influence*. PhD thesis, Delft University of Technology, 2015.



Appendix A: Airlift

CONFIDENTIAL

B

Appendix B: Multi Criteria Analysis

CONFIDENTIAL

B.1. Criteria & Grading System

CONFIDENTIAL

B.2. Weighting of the Criteria

CONFIDENTIAL

B.3. Normalization of the Weighing Factors

CONFIDENTIAL

B.4. Score Sheet MCA

CONFIDENTIAL

C

Appendix C: Python-program structure

CONFIDENTIAL



Appendix D: Mesh Independency Study

In the first part of this appendix the mesh generation that is used for the various numerical models is explained, the second part describes the inflation layers set up in the domain and the final part reviews issues encountered during the mesh generation.

D.1. Mesh Generation

As described in Chapter 7.2 the mesh used for the respective problem needs to ensure that the solution is independent of the mesh selected. To achieve this a mesh independency study is performed, during this study the two main aspects that are checked are whether the solution converges and if the solution is independent of the mesh.

Mesh independence is checked by comparing the CFD results of different mesh resolutions. One first starts with a certain mesh resolution and runs the simulation. Following this simulation another simulation is run for a finer mesh and this process is repeated several times. The results of the simulations are compared for the different meshes, see Figure D.1. It can be concluded that the solution is mesh independent when no significant deviation is observed in the simulation results when further refinement of the mesh is applied.

In order to consider the solution as converged it has to fulfill the following three conditions:

1. The residuals are monitored and checked whether they reduce to acceptable levels. Acceptable levels for the continuity, x-, y-, and z-velocity are set at 10^{-4} , whereas the residual values for the turbulent kinetic energy k and turbulent dissipation rate ϵ are less strict and allowed to have higher residual values;
2. Monitor points have been set up to check whether the solution has reached a steady state;
3. The imbalances in the simulation domain have to be less than 1 %.

In this case the mesh independency study is carried out for a free jet with the $k-\epsilon$ turbulence model and a SOD of $10 \cdot D$. The simulations for Mesh 1 and Mesh 2 did not meet the required residual levels and therefore further refinement of the mesh was applied. Continued refinement of the mesh ensured that the solution met the residual levels, the monitor points showed a steady state as can be seen in Figure D.2 ((for locations of the monitor points see Figure D.5) and imbalances in the domain stayed below 1 %. Looking at Figure D.1 Mesh 4 was chosen since further mesh refinement after Mesh 4 did not result in significant deviations in the results.

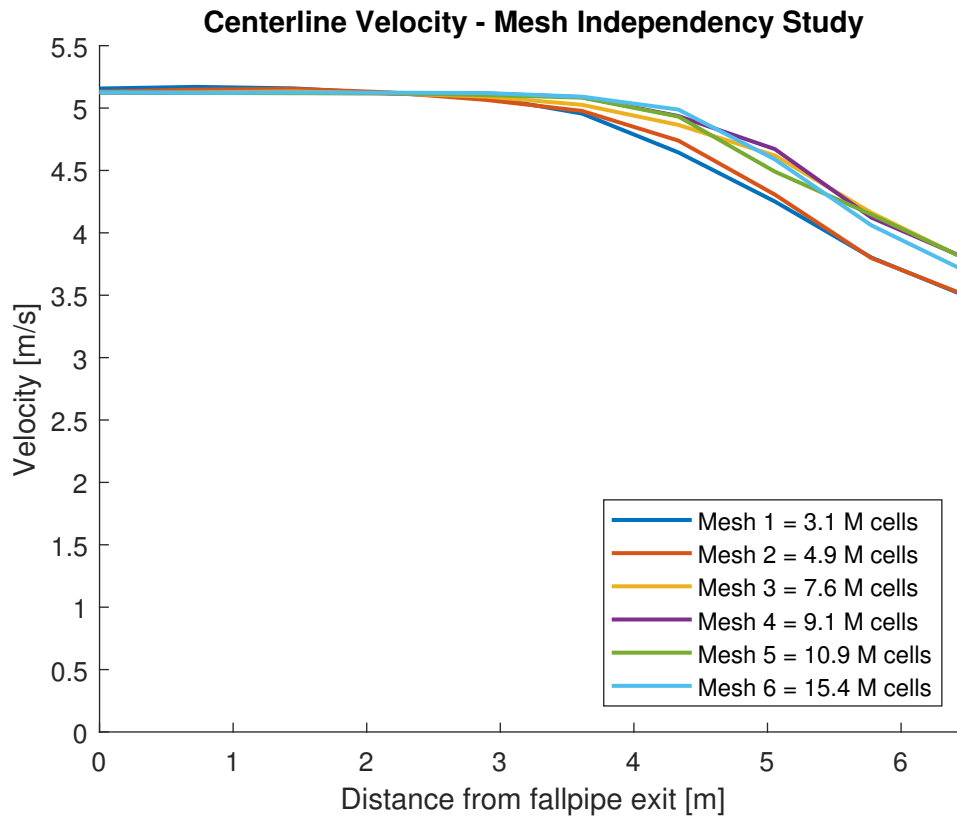
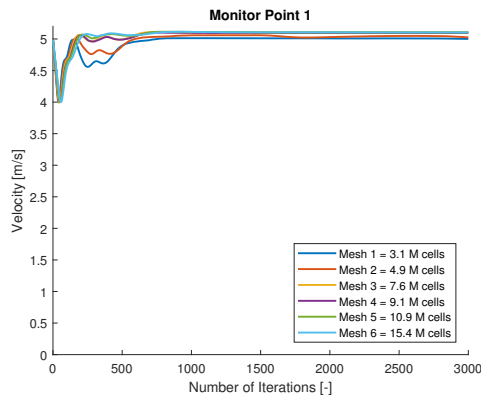
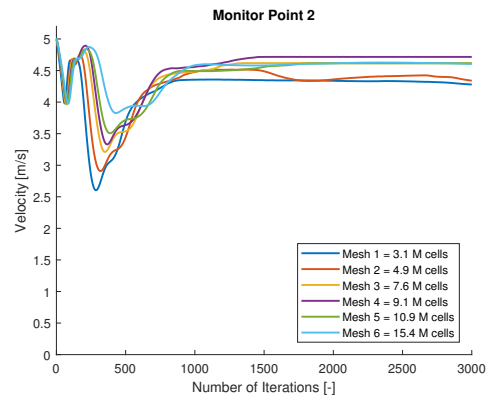


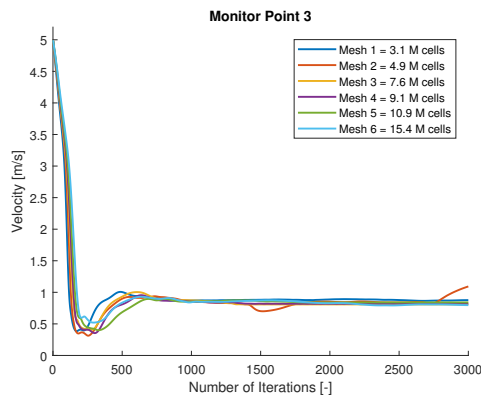
Figure D.1: Centerline Velocity - Mesh Independency Study



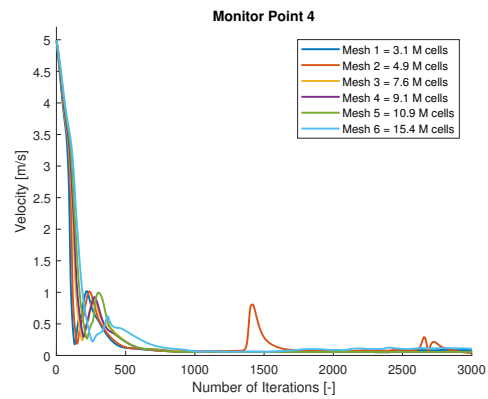
(a) Monitor Point 1 - Mesh Independence Study



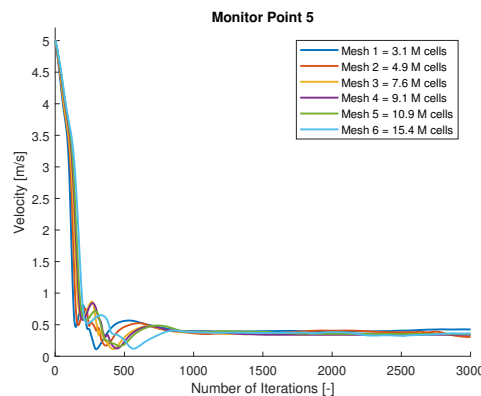
(b) Monitor Point 2 - Mesh Independence Study



(c) Monitor Point 3 - Mesh Independence Study



(d) Monitor Point 4 - Mesh Independence Study



(e) Monitor Point 5 - Mesh Independence Study

Figure D.2: Monitor Points - Mesh Independence Study

D.2. Near-Wall Treatment

In the near-wall region it is necessary to modify the model, since the presence of walls significantly affects turbulent flows. The near-wall region can be subdivided into three layers[Ferziger and Peric, 2002] [ANSYS, 2018a] with the log-law region in between the buffer layer and the outer layer, where the dimensionless wall distance y^+ for that respective layer is also represented :

- Viscous sublayer, $0 < y^+ < 5$: this is the innermost layer, viscous effects are dominant and the flow is almost laminar;
- Buffer layer, $5 < y^+ < 30$: this is the region between the outer layer and the viscous sublayer where neither the viscous and nor the turbulent effects are dominant, both play an equally important role;

- Log-law region, $30 < y^+ < 300$: in this region the viscous effects negligible and the turbulent shear stresses can be considered constant;
- Outer layer, $y^+ > 300$: this layer is the outer most layer of the near-wall region and turbulence is dominant here.

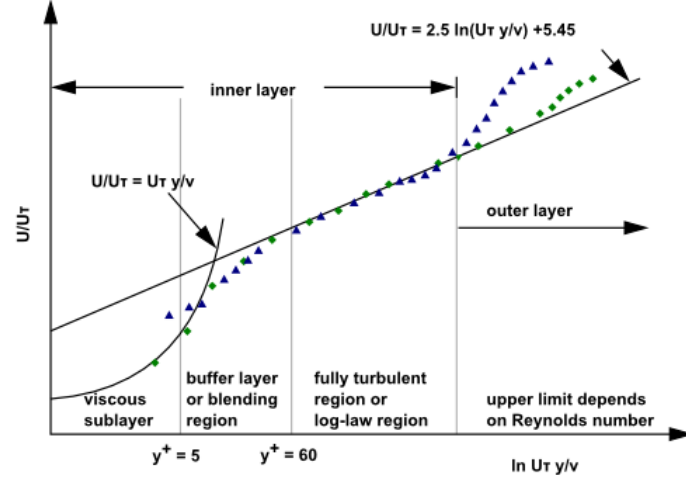


Figure D.3: Subdivisions of the near-wall regions [ANSYS, 2018a]

There are two main approaches to model this near-wall region. The first method is to bridge the viscosity affected region between the wall and the fully turbulent region, this is achieved with the use of semi-empirical formulas referred to as wall functions. The second method is to apply an extremely fine mesh near the wall to resolve the viscosity affected region properly. [ANSYS, 2018a] The former method, the use of wall functions, is the method used in this thesis. The first method allows tolerates a much coarser mesh in the near-wall region compared to the second method. This will result in lower computational power and time that is required to resolve the near-wall region. In order to use a wall function the velocity profile of a turbulent boundary layer has to obey the law-of-the-wall, meaning it has to be in the logarithmic region (log-law layer) [Ferziger and Peric, 2002]. The universal relation that represents the logarithmic velocity profile in the log-law layer is given by [Schlichting and Gerstein, 2000]:

$$u^+ = \frac{1}{\kappa} \ln y^+ + C^+ \quad (D.1)$$

Where u^+ is the dimensionless velocity, κ is the Von Kármán constant, y^+ is the dimensionless wall distance and C^+ is a constant generally dependent on the wall roughness. In order to ensure that the velocity profile of a turbulent boundary layer obeys the law-of-the-wall its y^+ value needs to be in the log-law layer, so $30 < y^+ < 300$. The chosen y^+ value in the log-law layer is used to compute the distance from the wall to the first cell in the mesh referred to as y_{wall} to obtain this chosen y^+ value. The procedure to compute this y_{wall} is as follows [CFD-online, 2011]:

Compute the Reynolds number:

$$Re = \frac{u_{inf} D}{\nu} \quad (D.2)$$

Estimate the skin friction coefficient [Schlichting, 1979] :

$$C_f = [2 \log_{10}(Re) - 0.65]^{-2.3} \quad \text{for } Re < 10^9 \quad (D.3)$$

Compute the wall shear stress:

$$\tau_w = C_f \frac{1}{2} \rho_w u_{inf}^2 \quad (D.4)$$

Compute the friction velocity:

$$u_* = \sqrt{\frac{\tau_w}{\rho_w}} \quad (D.5)$$

Compute the distance from the wall to the first cell:

$$y_{wall} = \frac{y^+ \mu}{\rho_w u_*} \tag{D.6}$$

For a chosen y^+ of 200 this gives a value of $y_{wall} = 0.00128 [m]$ that is set as first layer thickness in ANSYS Meshing on the wall boundaries. This layer has a growth rate of 1.2, the default setting in ANSYS Meshing, and 15 layers are applied since for unstructured meshes it is advised to us 10 to 20 layers. [ANSYS, 2018b]

D.3. Problems

The first coarse mesh simulations of the mesh independency study gave oscillating residuals (continuity, x-velocity, y-velocity, z-velocity, k and epsilon) which was expected, since the meshes were still too coarse. Further refinement of the meshes gave the expected result: the oscillations disappeared, and the residuals were stable and converged. However, for some of the refined meshes the oscillations in the residuals returned which was unexpected, see Figure D.4.

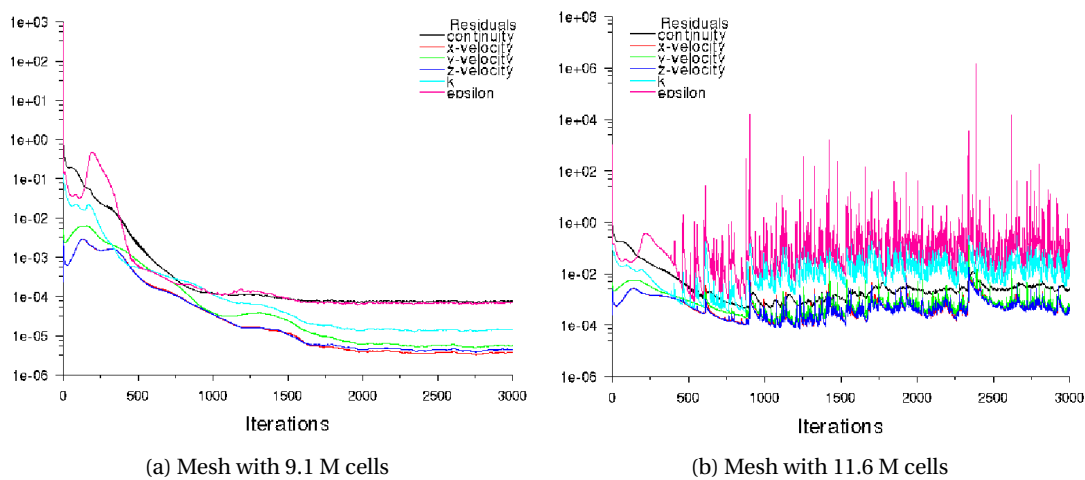


Figure D.4: Returning oscillating residuals for mesh refinement

To check whether a steady state was reached for these simulations with oscillating residuals the monitor point values were checked in the simulation domain. The location of these monitor points is the equal to the monitor point described in Appendix D.1 and visually presented in Figure D.5:

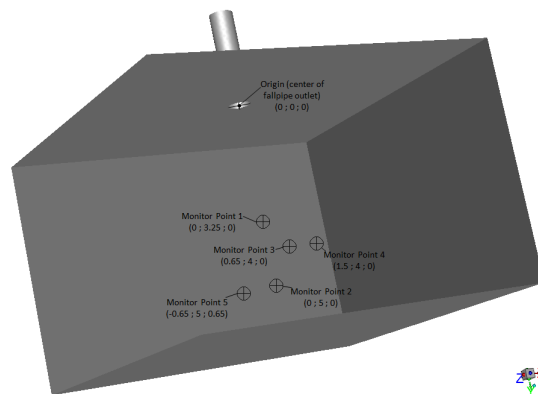


Figure D.5: Locations of the Monitor Points in the Simulation Domain

These monitor points measured the velocity magnitude at five different locations in the simulation domain and inspection of the monitor points demonstrated a steady state.

It was therefore concluded that the oscillatory behavior of the residuals of some of the fine meshes did not represent an unsteady solution. Possible causes for the incidental oscillatory behavior of the residuals are:

- The overall refinement of the mesh spread out over the entire simulation domain could result in the oscillations observed, due to the use of a very fine mesh in regions of virtually no flow movement;
- The free jet is not yet completely developed at the bottom boundary (pressure-outlet boundary condition FLUENT), this can cause problems at the boundary giving rise to high residual values at that specific location resulting in the oscillatory residuals;
- The way the residuals are calculated by FLUENT.

In order to check which one of the above-mentioned possibilities is the cause for the oscillatory behavior extra simulations are run. To check the first point a new mesh has been set up, this new mesh is refined along the centerline (refinement area has a radius of $2.5 \cdot D$ and continues until the bottom boundary see Figure D.6).

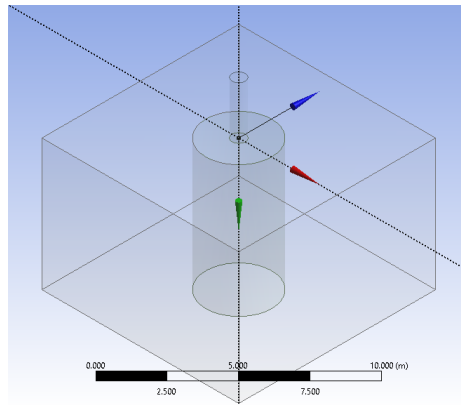


Figure D.6: Illustration of the local mesh refinement

Furthermore, simulations have been performed for an extended simulation domain, where the SOD is increased from $10 \cdot D$ to $15 \cdot D$ to check the second point, this is done for the new locally refined mesh and for the oscillatory mesh. Investigating the results from the locally refined meshes one could conclude that it damps out the oscillatory behavior, see Figures D.7a and D.7b. The application of a much coarser mesh in the regions of the flow where almost none to zero flow movement is present is most likely responsible for this result. However, the turbulent jet is not developing properly at the lower end of the flow domain, see Figure D.8a and D.8b, this is probably the reason for the sudden peaks in the residuals of the locally refined mesh and the small oscillations in the extended locally refined mesh. The way the refined mesh is set up is an explanation for the not properly developing turbulent jet. The mesh refinement could only be set up in separate sections that did not gradually progressed into each other. The knowledge level of an expert user of FLUENT is required to resolve this issue, however this cannot be obtained in the set time-frame.

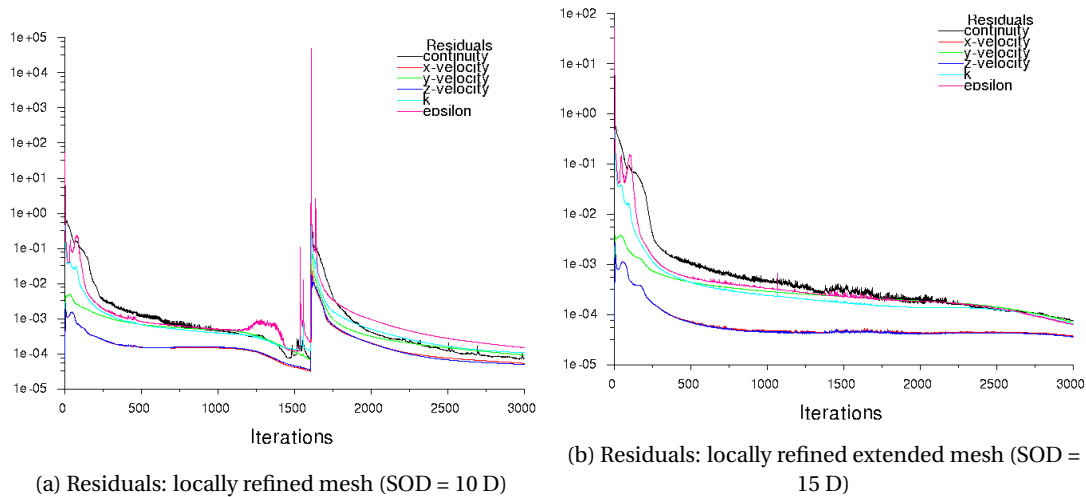


Figure D.7: Influence of local refinement on residuals

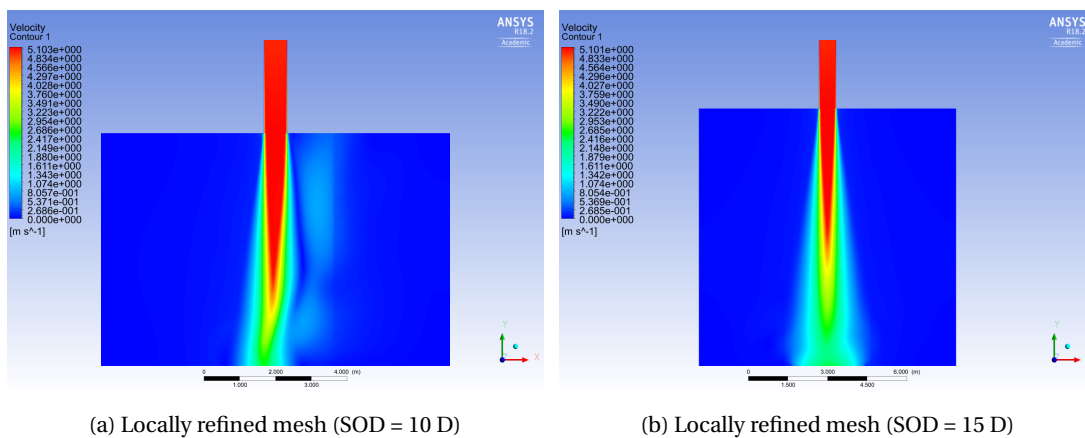


Figure D.8: Influence of local refinement on flow development

Analyses of the results for the extended simulation domain of the oscillatory mesh showed that the extension of the flow domain is not a solution for the oscillatory behavior, see Figure D.9.

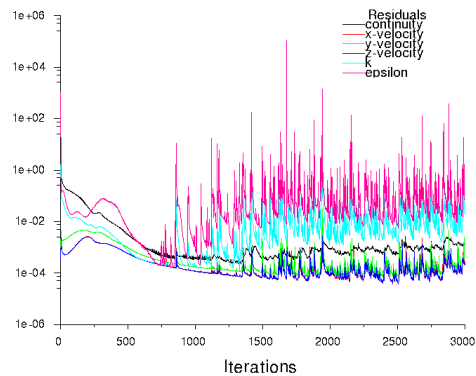
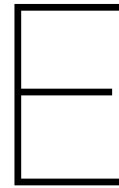


Figure D.9: Extended flow domain of oscillatory mesh (SOD = 15)

Investigation into the calculation method of the residuals in FLUENT pointed out that the calculation method used by FLUENT is not the cause of the oscillations [ANSYS, 2018b].

Finally, one could conclude that the oscillatory behavior of the residuals of certain meshes is caused by the use of a fine mesh in regions of low to none flow movement. In future research this can be resolved by gaining high-level knowledge of FLUENT. This will provide one with the right skills to create mesh refinements in the right areas whereas they will also grow gradually into a coarser mesh for areas of low to none flow movement.



Appendix E: Serial Numbers

Serial numbers for ANSYS FLUENT CFD simulations

First class			
A	Impinging Jet		
B	Deflector		
B - Sub-class			
Deflector angle [deg]			
B-A1	30.00		
B-A2	37.50		
B-A3	45.00		
B - Sub-sub-class			
Deflector length [m]		Deflector width [m]	
B-XX-L1	2.6	B-XX-LXW1	2.15
B-XX-L2	3.25	B-XX-LXW2	2.6875
B-XX-L3	1.95	B-XX-LXW3	1.6125
C	Diffuser		
FMIS	Free Jet Mesh Independency Study		
Second class			
The input velocity of the fallpipe flow.			
V1	2.5	[m/s]	
V2	5	[m/s]	
V3	7.5	[m/s]	
Third class			
The used turbulence model			
T0	no turbulence model		
T1	k-epsilon model		
T2	k-omegaSST model		
Fourth class			
The stand off distance from the orifice of the fallpipe to the seabed (with D the diameter of the fallpipe).			
S1	7.50 * D		
S2	10,0 * D		
S3	12.5 * D		
S4	15,0 * D		
S5	17.5 * D		
Fifth class			
The seabed roughness, there are 3 main seabed roughness values to be tested for, and 5 extra values that represent the roughness in the case the seabed is already covered with the respective rock grading.			
R0 Sub-class			
The default value of FLUENT for a smooth plate			
R1 Sub-class: the main seabed roughness heights			
	d ₅₀ [μm]	k _s [m]	
R1-1	100	0.00025	
R1-2	200	0.00050	
R1-3	400	0.00100	
R2 Sub-class: the main rock grading roughness heights			
	Grading	d ₅₀ [mm]	k _s [m]
R2-1	1-3"	40	0.1000
R2-2	1-4"	50	0.1250
R2-3	1-5"	60	0.1500
R2-4	1-8"	90	0.2250
R2-5	CP90/250	125	0.3125
Example code			
A_V1_T1_S2_R0			
Impinging Jet, 2.5 m/s, k-epsilon model, SOD = 10 D, default k _s			

Figure E.1: The different configurations of the CFD simulations with their respective serial numbers

F

Appendix F: Results CFD Simulations

In this appendix the results of all the simulations are plotted as future reference. The simulations performed are as follows:

- A_V2_T1_S2_R1-2
- A_V2_T1_S2_R2-3
- A_V2_T1_S4_R1-2
- A_V2_T1_S5_R1-2
- A_V2_T1_S5_R2-3
- A_V2_T2_S2_R1-2
- A_V2_T2_S5_R1-2
- A_V3_T1_S2_R1-2
- A_V3_T1_S5_R1-2
- B-A1-L1W1_V2_T1_S2_R1-2
- B-A1-L1W1_V2_T1_S4_R1-2
- B-A1-L1W1_V2_T1_S5_R1-2
- B-A1-L1W1_V2_T2_S2_R1-2
- B-A1-L1W1_V2_T2_S5_R1-2
- B-A1-L2W3_V2_T1_S2_R1-2
- B-A1-L3W2_V2_T1_S2_R1-2
- B-A1-L3W3_V2_T1_S2_R1-2
- B-A2-L1W1_V2_T1_S2_R1-2
- B-A3-L1W1_V2_T1_S2_R1-2
- B-A3-L1W1_V2_T1_S5_R1-2
- B-A3-L1W1_V2_T1_S5_R1-2_EXT (Same simulation settings as: B-A3-L1W1_V2_T1_S5_R1-2 only with a larger outflow domain)
- B-A3-L1W1_V2_T2_S2_R1-2

- B-A3-L1W1_V2_T2_S5_R1-2

Simulation results:

CONFIDENTIAL